Ocean Engineering 370 (2026) 129184



Contents lists available at ScienceDirect

Ocean Engineering

journal homepage: www.elsevier.com/locate/oceaneng



Research paper

Mooring tension prediction of floating offshore wind turbines under wind-wave-current misalignment with a transformer-inspired encoder-decoder architecture

Maokun Ye [a], Zhengrong Song [b], Xichong Yu [c], Decheng Wan [a,*]

[a] Computational Marine Hydrodynamics Lab (CMHL), School of Ocean and Civil Engineering, Shanghai Jiao Tong University, Shanghai, China
[b] Offshore Oil Engineering Co. Ltd, Tianjin, China
[c] CNOOC(China) Co. Ltd. Beijing New Energy Branch, Beijing, China

ARTICLE INFO

Keywords:
Floating offshore wind turbines (FOWTs)
Mooring
Neural networks
Transformer
Wind-wave-current misalignment

ABSTRACT

Real-time prediction of mooring line tension is critical for safeguarding the structural integrity and operational safety of floating offshore wind turbines (FOWTs). While machine learning has emerged as a promising alternative to computationally expensive coupled numerical simulations, most existing neural network (NN) models either assume perfectly aligned wind, wave, and current conditions or fail to effectively extract and utilize directional features even when these labels are included in training data, which severely restricts their generalization to unseen environmental angle combinations. To address this gap, we propose a Transformer-inspired encoder-decoder architecture that explicitly treats wind, wave, and current direction angles as dedicated inputs to the decoder branch. A cross-attention mechanism fuses temporal features from the encoder (historical six-degree-of-freedom platform motion and rotor thrust time series, serving as keys and values) with directional features from the decoder (serving as queries). Four NN models of progressively increasing complexity are developed and compared: a baseline GRU, a GRU-multi-head attention hybrid with concatenated direction features, and two encoder-decoder variants (full and simplified) differing in whether positional embedding is applied to static direction features. The models are validated using OpenFAST numerical simulations of the IEA 15 MW reference FOWT on the UMaine VolturnUS-S platform under a single parked load case with fixed environmental magnitudes and fixed wind-wave-current directions. On the interpolation test set, all models achieve R^2-scores above 0.92, with NN-1, NN-2, and NN-4 generally exceeding 0.95. On the extrapolation test set with unseen angular combinations, the encoder-decoder models (NN-3 and NN-4) maintain R^2-score and MAPE performance at levels similar to the interpolation set, whereas the baseline models (NN-1 and NN-2) exhibit significant accuracy degradation. Notably, the simplified encoder-decoder model (NN-4) outperforms the more complex full version (NN-3), indicating that excessive model complexity can lead to overfitting given the typically limited size of engineering training datasets. This work provides a promising direction for direction-aware mooring tension prediction; extension to time-varying directions and field-measured data is left for future work.

1. Introduction

Floating offshore wind turbines (FOWTs), which are essential for harnessing wind resources in deep-water regions, are restrained within a defined spatial range by their mooring systems, which play a critical role in ensuring the overall motion stability and structural safety of these platforms. Particularly under extreme environmental conditions, current loads can be extremely large, causing significant horizontal displacements of the floating platform and resulting in substantial tension forces in the mooring lines. When these large current loads are combined with the coupled nonlinear wind and wave loads acting on the floating turbine, they can induce sudden and abrupt changes in mooring line tension that may exceed the design safety thresholds.

For this reason, precise real-time prediction of mooring line tension in floating offshore wind turbines operating within complex marine environments is of critical importance for maintaining structural design integrity, ensuring operational safety, and achieving long-term economic sustainability. Traditional numerical methodologies rely on fully

* Corresponding author.
E-mail address: dcwan@sjtu.edu.cn (D. Wan).

https://doi.org/10.1016/j.oceaneng.2026.129184
Received 26 May 2026; Received in revised form 14 October 2026; Accepted 26 October 2026
Available online 30 October 2026
0029-8018/© 2026 Elsevier Ltd. All rights are reserved, including those for text and data mining, AI training, and similar technologies.

coupled aero-hydro-mooring simulations, where the dynamic behavior of mooring systems is described using either quasi-static or dynamic formulations. A detailed comparative analysis of these various modeling approaches lies outside the scope of the present investigation, and readers seeking such information are directed to the specialized review literature (Zhong et al., 2024). A fundamental characteristic of these simulations is that they require iterative solution processes within a tightly integrated computational framework. For example, determining the hydrodynamic loads exerted on FOWT platforms typically involves either potential flow theory or high-fidelity numerical techniques based on the Navier-Stokes equations.

Traditional high-fidelity computational fluid dynamics (CFD) approaches that directly solve the Navier-Stokes equations can theoretically deliver high levels of predictive accuracy, but their exorbitant computational requirements impose severe limitations on practical application (Wang et al., 2022a; Wang and Chen, 2023; Gu and Chen, 2024a, 2024b). For example, simulating a single combined wind-wave-current loading case may require multiple weeks of computational runtime. As a more efficient alternative, potential-flow-based coupled simulation frameworks, such as the aero-hydro-servo-mooring software developed by NLR (previously known as the National Renewable Energy Laboratory, NREL), have been extensively used to analyze the mooring tension characteristics of floating wind turbines.

Despite their proven effectiveness for controlled scenarios with clearly defined initial and boundary conditions, these coupled simulation techniques are only appropriate for mooring tension prediction during the design phase and cannot be deployed for real-world FOWT operations. This limitation stems from two key factors: (1) boundary conditions in actual marine environments are inherently indeterminate, as wind, wave, and current conditions are constantly evolving; and (2), their inherent computational inefficiency makes real-time prediction infeasible. Given these constraints, there is a pressing need for more computationally efficient methods for predicting mooring system tension to support the real-time operation and maintenance of floating offshore wind turbines.

Over the past decade, the rapid advancement of deep learning technologies, particularly artificial neural networks (ANNs), has opened transformative new avenues for addressing challenging prediction problems in marine engineering. An increasing number of researchers have applied these artificial intelligence techniques to the task of forecasting mooring line tension in floating offshore wind turbines. Unlike traditional numerical methods that rely on iterative solution of complex governing equations, ANNs possess the theoretical capability to approximate arbitrarily complex nonlinear mapping relationships between input and output variables. This fundamental property allows researchers to construct surrogate models for mooring system tension that can achieve accuracy levels comparable to the training data itself. Furthermore, once trained, neural networks (NN) essentially function as a sequence of linear algebra operations, enabling inference speeds that are orders of magnitude faster than conventional coupled numerical simulations. This unique combination of predictive accuracy and computational efficiency makes deep learning models particularly well-suited for real-time mooring tension prediction applications.

Predicting physical quantities such as FOWT platform motion responses and mooring line tensions represents a classic sequential modeling task in artificial intelligence, as these variables exhibit strong temporal dependencies that evolve continuously over time. Consequently, NN architectures specifically designed for processing sequential data have been widely adopted in this research domain. Among these, recurrent neural networks (RNNs) and their improved variants—including basic RNNs (Sherstinsky, 2020; Jin et al., 2025; Lee and Ahn, 2025), long short-term memory (LSTM) networks (Yu et al., 2019; Qiao et al., 2021; Halder et al., 2023; Yan et al., 2023; Deng et al., 2024; Zhang et al., 2024; Li et al., 2025), and gated recurrent unit (GRU) models (Chung et al., 2014a; Xie et al., 2023)—have emerged as the most prevalent choices. Payenda et al. (2024) conducted a comprehensive comparative analysis of GRU, LSTM, and bidirectional LSTM (Bi-LSTM) models for mooring dynamics prediction using platform motion measurements, emphasizing the critical importance of capturing bidirectional temporal relationships in the data. In a related study, Shi et al. (2023) developed a multi-input LSTM (MI-LSTM) framework that integrates platform motion, wave height, and mooring force data to forecast short-term surge motion, clearly demonstrating the performance benefits of incorporating multiple complementary temporal variables into the prediction model.

Although promising developments were achieved, RNN-based approaches still face notable challenges when applied to FOWT mooring tension prediction. A key limitation is their inherent difficulty in capturing long-range interdependencies among multivariate inputs—for example, the complex nonlinear correlations between incoming wind speed, significant wave height, and platform motion responses—that are essential for accurate mooring system analysis under complex marine conditions (Xu et al., 2022). To address these shortcomings and further improve prediction accuracy, researchers have explored a variety of supplementary techniques. One widely adopted strategy involves preprocessing input signals by applying filtering methods or decomposing them into distinct long- and short-period components based on prior knowledge of the frequency-domain characteristics of mooring system responses (Yao et al., 2022; Ye et al., 2022; Chen et al., 2022, 2025; Xie and Tang, 2024; Hu et al., 2025). Another active research direction focuses on developing hybrid NN architectures that combine the complementary strengths of different model types. For instance, hybrid models integrating RNNs with convolutional neural networks (CNNs) have been proposed to enhance feature extraction capabilities. Yuan et al. (2023) introduced a sophisticated hybrid VMD-CNN-LSTM/CNN-BiLSTM framework that uses variational mode decomposition (VMD) to effectively handle the nonlinear and non-stationary nature of mooring tension data, combined with an integrated error correction mechanism to further boost prediction performance. Numerous other investigations have also followed similar hybrid modeling paradigms to achieve improved results in mooring tension forecasting (Zhao et al., 2023; Gong et al., 2024; Tang et al., 2025; Song et al., 2025).

In recent years, the Transformer architecture (Vaswani et al., 2017)—originally pioneered in the field of large language models—has been successfully extended to mooring tension prediction applications for floating offshore platforms. The defining advantage of Transformer models stems from their core attention mechanism, which enables them to theoretically capture global dependencies across all elements of an input sequence regardless of their temporal distance. This unique capability has established Transformer-based approaches as exceptionally promising solutions for time-series forecasting problems in marine engineering. Yuan et al. (2024) developed an enhanced Transformer framework specifically for real-time ultra-short-term mooring tension prediction on the “DeepSea One” semi-submersible production platform. In their implementation, the encoder processes historical mooring tension time series augmented with positional encoding, while the decoder takes a shifted version of the target mooring tension sequence (also incorporating positional encoding) as input. Their comparative analysis revealed that the proposed Transformer model outperformed mainstream LSTM networks across multiple performance metrics, delivering superior prediction accuracy, enhanced robustness, and improved generalization capability. These advantages were particularly pronounced for multi-step forecasting horizons ranging from 3 to 15 s under various sea conditions. Building on this progress, Ma et al. (2026) introduced a Transformer-based approach integrated with Gaussian process-driven Bayesian optimization to address the challenge of high-precision mooring tension prediction for FOWTs during non-stationary typhoon transit events. Their model's encoder accepts time-series data of non-stationary typhoon environmental loads—including wind speed and key wave

parameters—supplemented with positional encoding. The corresponding decoder processes a shifted sequence of historical mooring tension values, also enhanced with positional encoding. The research demonstrated that this integrated framework achieved significantly higher prediction accuracy than traditional LSTM-SA models, exhibited excellent generalization performance on previously unseen sea states, and possessed a stronger ability to capture the extreme nonlinear dynamic responses that occur during typhoon conditions.

Despite the remarkable computational efficiency of NN-based mooring tension prediction approaches, a fundamental limitation remains pervasive in existing research: the vast majority of studies do not explicitly account for wind-wave-current directionality, meaning these critical angular features are either omitted or merely concatenated as passive inputs during model training. This is particularly problematic because mooring tension responses are highly sensitive to environmental incident angles—misalignment between wind, wave, and current can significantly alter platform motion responses and tension distributions. Consequently, models trained without explicit direction awareness suffer from severe performance degradation when generalized to out-of-distribution (OOD) angular combinations not seen during training. Xie et al. (2023) developed deep gated recurrent unit (GRU) networks for long-term fatigue analysis of mooring lines that account for wave directionality by incorporating wave surface elevation components as model inputs. Xie and Tang (2024) further proposed a domain generalization approach for mooring tension prediction across varying environmental conditions. Nevertheless, in these studies directionality is either implicitly encoded through wave elevation inputs or handled via domain adaptation, rather than as an explicit, dedicated decoder feature. Furthermore, no existing study systematically evaluates extrapolation performance on completely unseen wind-wave-current angular combinations, i.e., directional out-of-distribution (OOD) conditions.

Through our prior research (Ye et al., 2026), we found that prediction methods relying exclusively on platform six-degree-of-freedom (6-DoF) motion time series—without explicitly modeling environmental load directions—exhibit significant performance degradation when generalized to previously unseen wind-wave-current incidence angles. As a natural extension of our earlier work, this study addresses this critical gap by developing a direction-aware NN architecture that efficiently learns directional characteristics from limited datasets. To the best of our knowledge, this is the first study to integrate wind-wave-current direction angles as independent decoder inputs with cross-attention in a Transformer-inspired encoder-decoder architecture for mooring tension prediction under directional OOD conditions.

The primary objective of this study is to develop a direction-aware encoder-decoder model for mooring tension prediction that explicitly treats wind, wave, and current direction angles as dedicated decoder inputs, and to systematically evaluate its interpolation and extrapolation (out-of-distribution) generalization against baseline models without such a direction-aware design. In addition, this work also assess how architectural complexity interacts with the typically limited size of engineering training datasets, by comparing the full and simplified encoder-decoder variants. Therefore, in this work, we systematically develop and compare four NN models with progressively increasing complexity to rigorously evaluate the effectiveness of our proposed approach.

- The first model (NN-1) is a standard GRU network, which serves as our baseline benchmark. Widely adopted for time-series forecasting in marine engineering applications, this model only processes historical time-series data of platform motion responses and rotor thrust, without incorporating any wind-wave-current direction information.
- The second model (NN-2) is a GRU-MHA hybrid architecture that integrates the multi-head attention (MHA) mechanism—the core component of Transformer models—into the GRU framework. In this encoder-only design, wind-wave-current direction angles are directly concatenated with the motion and thrust time series as inputs to the network.
- The third and fourth models (NN-3 and NN-4) are the two new encoder-decoder architectures proposed in this study, both adapted from the Transformer framework originally developed for large language models. Both models employ a dual-branch design: the encoder branch processes historical time-series data of the platform's 6-DoF motions and rotor thrust, while the decoder branch takes the individual wind, wave, and current direction angles as separate inputs. A key innovation of these architectures is the cross-attention mechanism, where the encoder-processed motion and thrust features serve as the keys (K) and values (V), and the decoder-processed direction features serve as the queries (Q). This cross-attention mechanism enables effective fusion of temporal motion information and static directional information, allowing the model to explicitly learn directional patterns from the training data. The only distinction between NN-3 (Enc-Dec-Full) and NN-4 (Enc-Dec-Simplified) lies in the treatment of directional features: NN-3 fully incorporates the positional embedding mechanism from the original Transformer architecture, while NN-4 simplifies this structure by directly feeding static direction features into the decoder without positional encoding.

The main contributions and novelties of this work can be summarized as follows.

1. A direction-aware encoder-decoder architecture is proposed in which wind, wave, and current direction angles are fed as independent inputs to the decoder branch. Unlike previous studies that either ignore directional information or simply concatenate it with temporal inputs, this design explicitly separates static directional features from dynamic temporal features, enabling the model to comprehensively understand the complex nonlinear relationships between platform dynamic responses and environmental load directions.
2. The proposed encoder-decoder models, which explicitly incorporate wind-wave-current directionality, exhibit robust adaptability to various combinations of environmental load angles. A systematic extrapolation evaluation on completely unseen wind-wave-current angular combinations demonstrates that the proposed models maintain stable prediction performance under OOD conditions, whereas baseline models without direction-aware decoding exhibit significant degradation. This capability makes them particularly suitable for mooring tension forecasting under conditions where wind, wave, and current directions differ from those seen during training.
3. Contrary to common intuition, the simplified encoder-decoder model (NN-4) outperforms the more complex full version (NN-3), indicating that larger and more complex models do not necessarily yield better performance when the available engineering training dataset is limited. The corresponding quantitative evidence and physical explanation are provided in Sections 5.3 and 6.

The organization of the remainder of this manuscript is outlined below: Section 2 presents the detailed methodology of this study, starting with an introduction to the fundamental NN components that form the building blocks of our models, followed by a comprehensive description of the four proposed architectures with progressively increasing complexity. Section 3 describes the test case setup, including the specifications of the IEA 15 MW reference floating offshore wind turbine, the numerical modeling approach for simulating fully coupled FOWT dynamic responses under combined wind-wave-current loads, and the definition of environmental loading cases used for generating the training and testing datasets. Section 4 details the model training process, covering the specialized dataset splitting strategy designed to

separately evaluate interpolation and extrapolation performance, as well as the training specifications and hyperparameter configurations employed in this work. Section 5 provides a systematic evaluation and in-depth discussion of the experimental results, comparing the performance of the four models across three distinct test datasets that assess time-series prediction accuracy, interpolation capability within the training parameter range, and generalization to previously unseen wind-wave-current angles. Finally, Section 6 summarizes the key findings of this study, highlights the main scientific contributions, discusses the limitations of the current work, and outlines promising directions for future research in this field.

2. Methodology

2.1. General statement of NN models in this work

This chapter begins by introducing the fundamental building blocks that constitute the four neural network (NN) architectures developed in this study. We then present a detailed description of the four NN frameworks proposed for floating offshore wind turbine mooring tension prediction, organized in order of progressively increasing architectural complexity. The development sequence starts with the baseline gated recurrent unit (GRU) model (NN-1), followed by the GRU-multi-head attention (GRU-MHA) hybrid model (NN-2) which represents an encoder-only design. We next introduce the full Transformer-inspired encoder-decoder model incorporating positional embedding (NN-3). Building on this complete architecture, we eliminate the structural components that increase computational complexity without adding meaningful physical information, yielding a streamlined Simplified Encoder-Decoder model, designated as NN-4. The overall hierarchical design philosophy and comparative architecture of the four NN models developed in this work are schematically illustrated in Fig. 1.

2.2. Basic architecture components

Complex NN architectures are typically constructed by combining and integrating a set of fundamental, reusable building blocks. Understanding these foundational elements is essential for comprehending the design principles and structural differences between the various models developed in this study. In this section, we first describe the core basic components that are utilized to construct all four NN models presented in this work.

2.2.1. Multi-layer perceptron (MLP)

The Multi-Layer Perceptron (MLP) is the most fundamental building block of modern neural networks and is ubiquitously integrated with other components to construct complex architectures, where it is used to reshape input and output tensors, adjust feature dimensions, and perform final regression or classification tasks. Its overall structure and the transformations within a single neuron are illustrated in Fig. 2. All fully connected layers in this study incorporate residual connections to enhance training efficiency and alleviate the vanishing gradient problem (He et al., 2015).

2.2.2. Gated recurrent units (GRU)

The Gated Recurrent Unit (GRU) (Chung et al., 2014b), an enhanced variant of recurrent neural networks (RNNs), overcomes the limitations of standard RNNs in processing sequential and time-series data through its gating mechanism. In marine engineering, GRUs have been widely applied to predict dynamic structural responses such as mooring line tensions and platform motions of floating offshore wind turbines (FOWTs). The gating mechanism adaptively controls the flow of information, deciding which historical information to retain and which new information to incorporate, thereby mitigating the vanishing gradient problem and enabling the learning of long-range dependencies. This makes GRUs well suited to capturing both the high-frequency wave-induced oscillations and the low-frequency slow-drift motions that dominate FOWT responses, including during extreme storm events. The fundamental mathematical expressions of the GRU model are:

$$z_t = \sigma(W_z \cdot [h_{\{t-1\}}, x_t] + b_z) \tag{1}$$

$$r_t = \sigma(W_r \cdot [h_{\{t-1\}}, x_t] + b_r) \tag{2}$$

$$\widetilde{h}_t = \tanh(W_h \cdot [r_t \odot h_{\{t-1\}}, x_t] + b_h) \tag{3}$$

$$h_t = (1 - z_t) \odot h_{\{t-1\}} + z_t \odot \widetilde{h}_t \tag{4}$$

Equations (1)–(4) define the complete mathematical operations within each GRU cell. Here, t denotes the current time step, x_t represents the input feature vector at time t (including platform 6-DoF motions and rotor thrust in our task), and h_{t-1} is the hidden state from the previous step that encodes accumulated historical information. Two gating units regulate information flow: the update gate z_t (bounded to [0,1] by the sigmoid function σ determines how much of the previous hidden state is retained, while the reset gate r_t (also in [0,1]) controls the influence of past information on the new candidate hidden state $\widetilde{h}_t$. The weight matrices W_z, W_r, W_h and bias vectors b_z, b_r, and b_h are adjusted in the training process. The notation [,] denotes vector concatenation, $\odot$ represents element-wise multiplication, and the tanh function maps values to [−1,1] for stable training. The candidate hidden state $\widetilde{h}_t$ is computed based on the current input and gated historical information. The final hidden state h_t is a weighted combination of h_{t-1} and $\widetilde{h}_t$ (weighted by z_t), serving as both the cell output at time t and the memory state for the next time step. A schematic overview of the overall GRU network architecture is presented in Fig. 3(a), while the detailed internal structure and computational operations within a single GRU cell are illustrated in Fig. 3(b).

2.2.3. Multi-head attention (MHA)

As the cornerstone component of the Transformer architecture (Vaswani et al., 2017), the Multi-Head Attention (MHA) mechanism overcomes a key limitation of traditional RNNs: their difficulty in capturing long-range dependencies. Unlike RNNs that process sequences

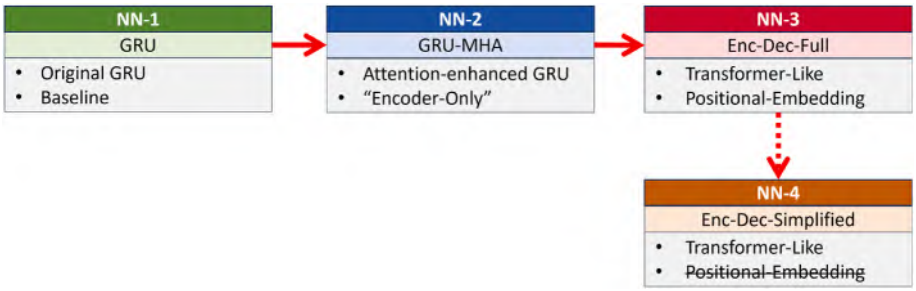

Fig. 1. Proposed NN models in the study.

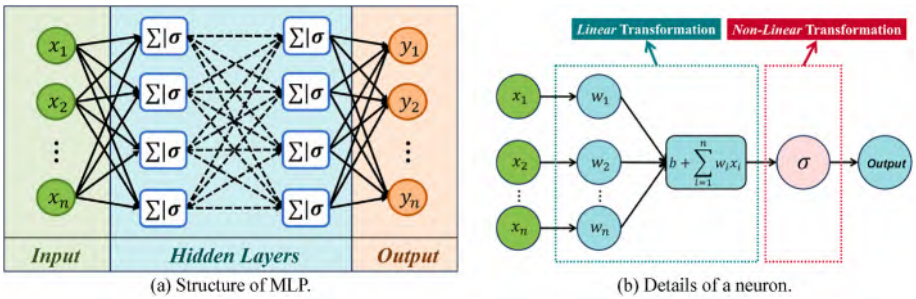

(a) Structure of MLP. (b) Details of a neuron.

Fig. 2. Illustration of MLP.

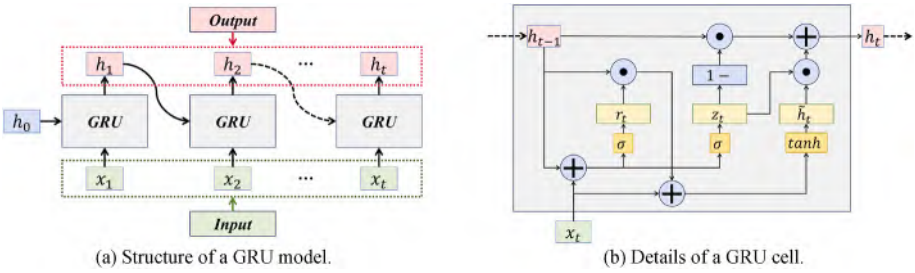

(a) Structure of a GRU model. (b) Details of a GRU cell.

Fig. 3. Illustration of GRU.

sequentially, MHA captures interactions between any elements of a sequence irrespective of their temporal distance, which makes it well suited to uncovering the complex nonlinear interactions that govern FOWT mooring responses. The core idea of MHA is to decompose the attention computation into multiple parallel, independent "attention heads" rather than relying on a single attention function, allowing the model to attend to information from distinct representation subspaces simultaneously. For example, one head may capture short-term, high--frequency correlations induced by incident waves, while another focuses on long-term trends in wind loading or the resonant responses of the floating platform. The mathematical formulation of the MHA mechanism is expressed by the following equations:

$$Attention(Q,K,V) = softmax\left(\frac{Q\cdot K^T}{\sqrt{d_k}}\right)\cdot V \tag{5}$$

where:

$$Q = X\cdot W_Q \tag{6}$$

$$K = X\cdot W_K \tag{7}$$

$$V = X\cdot W_V \tag{8}$$

Then, MHA can be expressed as:

$$head_i = Attention\left(X\cdot W_{Q_i}, X\cdot W_{K_i}, X\cdot W_{V_i}\right) \tag{9}$$

$$MultiHead(X) = \boldsymbol{Concat}(head_1, head_2, \ldots, head_h)\cdot W_O \tag{10}$$

The mathematical formulation (Eq. (5) to Eq. (10)) of the MHA mechanism relies on a set of key variables and operations, which are defined below. The input to the MHA module is represented by matrix $\boldsymbol{X}$, which contains the sequential feature vectors extracted from the input data. At the core of the attention computation are three fundamental matrices: the Query matrix ($\boldsymbol{Q}$), which encodes what information the model is seeking to retrieve; the Key matrix ($\boldsymbol{K}$), which provides unique identifiers for matching against the queries; and the Value matrix ($\boldsymbol{V}$), which contains the actual content to be extracted based on the query-key similarity scores. These three matrices are derived by projecting the input $\boldsymbol{X}$ through three separate learnable weight matrices, denoted as W_Q, W_K, and W_V respectively. Here, d_k represents the dimensionality of each Query and Key vector, while h denotes the total number of parallel attention heads operating simultaneously. For each individual attention head i, dedicated projection matrices W_{Q_i}, W_{K_i}, W_{V_i} are used to generate head-specific $\boldsymbol{Q}$, $\boldsymbol{K}$, and $\boldsymbol{V}$ representations, producing the intermediate output $head_i$. Once all attention heads have computed their outputs, they are concatenated together using the Concat operation, and the resulting combined feature vector is projected through a final learnable weight matrix W_O to produce the unified output of the MHA module. A schematic diagram illustrating the overall structure of the MHA module is provided in Fig. 4(a), while the detailed computational flow within a single attention head is shown in Fig. 4(b).

2.3. Proposed NN models

2.3.1. GRU (NN-1): The original GRU model

The first NN model developed in this study is a standard gated recurrent unit (GRU) architecture, which has become the most widely adopted NN framework for predicting floating platform motion responses and mooring line tensions in contemporary marine engineering research. We employ this well-established model as our fundamental baseline to establish a performance reference for evaluating the more advanced architectures proposed in subsequent sections. The input-output mapping relationship implemented by the NN-1 model is formally defined in Eq. (11). In this baseline configuration, the wind direction (wdd), wave direction (wvd), and current direction (crd) variables are tiled to match the length of the historical input sequence, and then incorporated as three additional feature channels into the GRU network alongside the platform motion and rotor thrust time series.

$$Mooring\ Tensions^t = \mathcal{NN}1\left(surge^{his}, sway^{his}, heave^{his}, roll^{his}, pitch^{his}, yaw^{his}, thrust^{his}, wdd, wvd, crd\right) \tag{11}$$

The architectural schematic of the NN-1 baseline model is presented in Fig. 5. The output layers of all four NN models developed in this study share an identical design, consisting of a multi-layer perceptron (MLP) that performs dimensionality reduction and nonlinear regression to generate the final mooring tension predictions. Prior to feeding data into the NN, two preprocessing steps are applied consistently across all

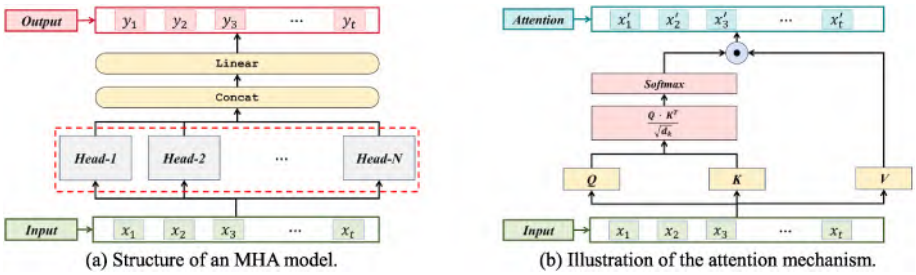

(a) Structure of an MHA model. (b) Illustration of the attention mechanism.

Fig. 4. Illustration of MHA.

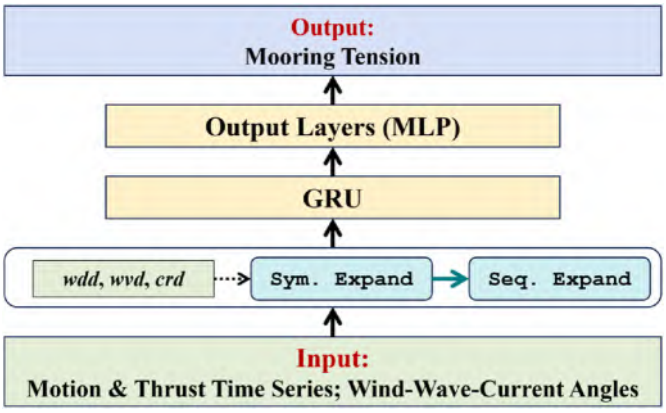

Fig. 5. Structure of the NN-1 model.

models to ensure controlled comparison and leverage physical insights. The first step, denoted as "Symmetric Expansion", is a physics-informed feature engineering technique that exploits the axisymmetric nature of the target floating offshore wind turbine platform. This fundamental geometric property dictates that for identical wind, wave, and current magnitudes, mooring tension responses will exhibit rotational symmetry when environmental load directions are rotated around the platform's central vertical axis. By applying this symmetric transformation to the input data, we effectively augment the training dataset while preserving the underlying physical relationships governing system behavior. Following symmetric expansion, the static wind, wave, and current direction features are extended to match the length of the historical time-series inputs through a "Sequential Expansion" operation (denoted as Sym. Expand in Fig. 5). This ensures that all input features have consistent temporal dimensions, which is a prerequisite for processing by time-series NN architectures. These two preprocessing pipelines are implemented uniformly across all four models in this study to isolate the performance differences arising exclusively from architectural variations rather than data preparation strategies.

2.3.2. GRU-MHA (NN-2): An encoder-only model

The second NN model, designated as NN-2, integrates a standard GRU backbone with a multi-head attention (MHA) module to enhance its ability to capture complex temporal dependencies. In this configuration, the query (Q), key (K), and value (V) matrices are all derived exclusively from the input sequence itself, making this a strictly self-attention implementation. As the core component of Transformer architectures, MHA enables the model to explicitly extract and quantify correlations between any two elements in the input sequence, regardless of their temporal separation. This capability has been widely demonstrated in previous studies to improve prediction performance across various time-series forecasting tasks. We include this GRU-MHA hybrid model as our second benchmark to isolate the performance improvements attributable to the attention mechanism itself, allowing us to rigorously evaluate whether the gains observed in our proposed encoder-decoder architectures stem from the attention mechanism or from the novel encoder-decoder structural design. The input-output mapping relationship implemented by the NN-2 model is formally defined in Eq. (12). Consistent with the NN-1 baseline, the wind direction (*wdd*), wave direction (*wvd*), and current direction (*crd*) features are tiled to match the length of the historical input sequence and incorporated as additional input channels alongside the platform motion and rotor thrust time series. The complete architectural schematic of the NN-2 model is provided in Fig. 6.

$$Mooring\ Tensions^{t} = \mathcal{NN}2\left(surge^{his}, sway^{his}, heave^{his}, roll^{his}, pitch^{his}, yaw^{his}, thrust^{his}, wdd, wvd, crd\right) \tag{12}$$

2.3.3. Enc-Dec-Full (NN-3): A transformer-inspired encoder-decoder model with positional embedding

The Transformer architecture (Vaswani et al., 2017), originally developed for natural language processing tasks, is built around a powerful encoder-decoder framework that has revolutionized sequence-to-sequence modeling. This framework consists of two distinct, specialized modules: the encoder processes the source input sequence to extract comprehensive contextual representations, while the decoder generates the target output sequence by conditioning on both the encoder's outputs and task-specific target information. This separation of input processing and output generation makes the encoder-decoder architecture particularly well-suited for problems where input features belong to different categories or exhibit fundamentally different characteristics.

The third NN model in this study, designated as NN-3 (Enc-Dec-Full), is a customized adaptation of this Transformer-like encoder-decoder architecture specifically designed for FOWT mooring tension prediction, with its complete structure illustrated in Fig. 7. The input-output

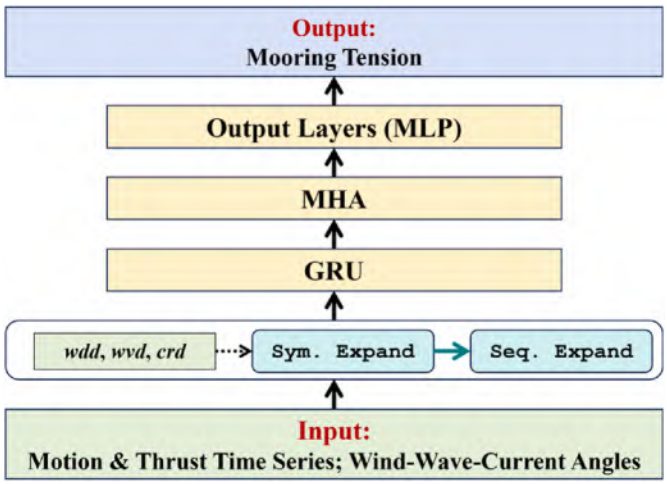

Fig. 6. Structure of the NN-2 model.

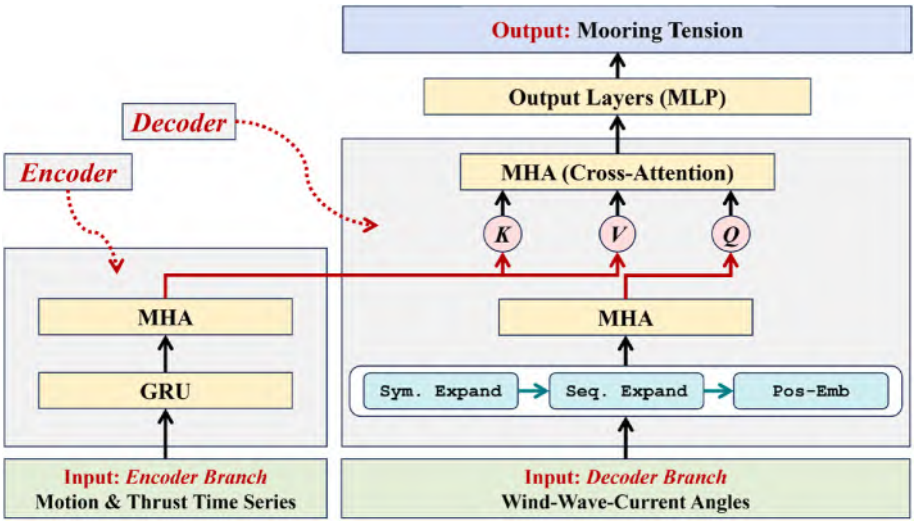

Fig. 7. Structure of the NN-3 model.

mapping relationship implemented by NN-3 is formally defined in Eq. (13). A key innovation of this architecture compared to the previous benchmark models is its dual-branch input design, which explicitly separates different types of input features. As shown in Eq. (13), the model receives two distinct sets of inputs: the first set comprises the historical time-series data of the platform's six-degree-of-freedom motions and rotor thrust, which are fed exclusively into the encoder branch to extract temporal dynamic features; the second set consists of the wind direction (*wdd*), wave direction (*wvd*), and current direction (*crd*) features, which are dedicated inputs to the decoder branch. Consistent with the processing pipeline used in the benchmark models, these three static directional features are extended to match the length of the historical time-series inputs to ensure dimensional alignment for subsequent cross-attention computations.

$$Mooring\ Tensions^{t} = \mathcal{NN}3\Big(\Big[surge^{his}, sway^{his}, heave^{his}, roll^{his}, pitch^{his}, yaw^{his}, thrust^{his}\Big]; [wdd, wvd, crd]\Big) \tag{13}$$

As illustrated in Fig. 7, the directional inputs to the decoder branch—wind direction (*wdd*), wave direction (*wvd*), and current direction (*crd*)—undergo a three-stage processing pipeline before entering the cross-attention module. First, the symmetric expansion operation is applied to leverage the axisymmetric property of the FOWT platform, identical to the preprocessing step used in the benchmark models. Following this, the static directional features are extended through sequential expansion to match the temporal length of the platform motion and rotor thrust time series, ensuring dimensional consistency between the encoder and decoder inputs. Finally, the expanded directional sequences are processed through a positional embedding layer. The positional embedding mechanism was originally introduced in the Transformer architecture to address a fundamental limitation of pure attention mechanisms: their inherent permutation invariance, which means they cannot inherently distinguish the order of elements in a sequence. Since attention operations treat all positions equally regardless of their temporal location, explicit positional information must be injected into the input representations to enable the model to capture sequential dependencies. In this study, we employ the standard sine-cosine positional encoding scheme from the original Transformer paper, which provides fixed, continuous positional representations that generalize well to sequence lengths not encountered during training. The detailed mathematical formulation of this positional encoding method can be found in the original work of Transformer (Vaswani et al., 2017).

2.3.4. Enc-Dec-Simplified (NN-4): A simplified transformer-like encoder-decoder model

The fourth NN model, designated as NN-4 (Enc-Dec-Simplified), is a streamlined variant derived directly from the full Enc-Dec-Full (NN-3) architecture. This simplified design was developed to eliminate non-essential structural components that increase computational complexity without contributing meaningfully to prediction performance for our specific mooring tension forecasting task. Importantly, NN-4 retains all the core architectural innovations of the NN-3 model, including the dual-branch encoder-decoder structure and the cross-attention mechanism that enables effective fusion of temporal dynamic features and directional environmental features. The input-output mapping relationship implemented by the NN-4 model is formally defined in Eq. (14).

$$Mooring\ Tensions^{t} = \mathcal{NN}4\Big(\Big[surge^{his}, sway^{his}, heave^{his}, roll^{his}, pitch^{his}, yaw^{his}, thrust^{his}\Big]; [wdd, wvd, crd]\Big) \tag{14}$$

A critical insight that motivated the development of the NN-4 model relates to the fundamental nature of the wind-wave-current directional features used in this study. Unlike the platform motion and rotor thrust time series, which exhibit dynamic temporal variations, the directional parameters (*wdd-wvd-crd*) are inherently static features within each individual simulation case. When generating our dataset, each numerical simulation is performed under fixed environmental conditions, meaning the wind, wave, and current directions remain constant throughout the entire simulation period. Consequently, when these static directional values are expanded to match the length of the historical time series, they form sequences where every time step contains exactly the same value.

Given this temporal invariance, the positional embedding layer employed in the NN-3 model serves no meaningful purpose for the directional input branch. The original positional embedding mechanism was designed to inject temporal order information into sequences where element position carries semantic meaning. However, applying positional encoding to a sequence of identical values only introduces artificial, spurious variations that have no physical basis in the actual problem. This unnecessary operation not only significantly increases model complexity and computational overhead but also introduces irrelevant noise into the cross-attention computation, which can degrade learning efficiency and potentially hinder prediction performance. Based on this physical reasoning and empirical observation, we removed the positional embedding layer entirely from the decoder

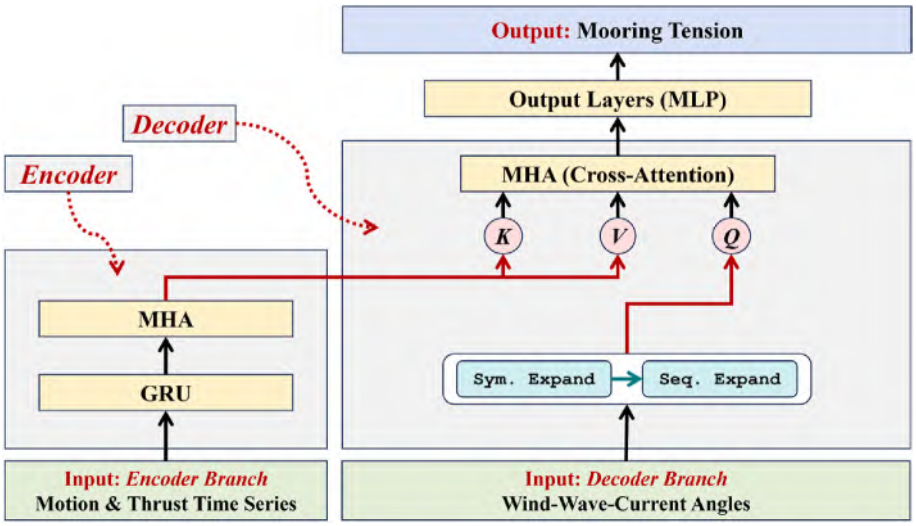

Fig. 8. Structure of the NN-4 model.

branch, resulting in the streamlined Enc-Dec-Simplified (NN-4) architecture, whose complete structure is illustrated in Fig. 8.

3. Test case description

Rigorous validation using realistic test cases and high-quality datasets is essential for evaluating the performance and generalization capability of machine learning models in engineering applications. In this section, we present a detailed description of the reference floating offshore wind turbine (FOWT) platform used in this study, the numerical modeling approach employed to simulate its dynamic responses under various ocean environmental conditions, and the systematic data generation process used to construct the training, validation, and test datasets for evaluating the four NN architectures developed in this work.

3.1. The reference FOWT

This research selects the IEA 15 MW floating offshore wind turbine as the numerical research model (Gaertner et al.). This advanced model acts as a standard prototype for large-scale offshore wind facilities, and is tailored to operate in deep sea areas. The wind turbine possesses a rated power of 15 MW, with a rotor diameter of roughly 240 m and a hub height of 150 m. The whole unit is installed on the UMaine VolturnUS-S semi-submersible floating platform (Allen et al., 2020), whose structural design guarantees stable operation when exposed to severe marine surroundings. Widely adopted in relevant academic studies, this reference turbine is well applicable to analyze structural dynamic characteristics and mooring system performance under coupled environmental loads. The overall layout of the wind turbine and matching mooring arrangement can be seen in Fig. 9. To keep the content concise, detailed dimensional data and design parameters of the model can be found in the official public document released by NLR (Allen et al., 2020).

3.2. Numerical modeling of dynamic responses of FOWTs under wind-wave-current loadings

The dynamic behaviors of the IEA 15 MW wind turbine installed on the UMaine VolturnUS-S semi-submersible platform are calculated with OpenFAST (Jonkman, 2007; Rinker et al., 2020; Wang et al., 2022b). This open-source high-precision simulation program is developed by NLR, and it is capable of conducting fully coupled analysis covering aerodynamic, hydrodynamic, control and structural elastic characteristics of floating wind turbines under actual marine working conditions. Blade element momentum theory is adopted to calculate aerodynamic loads acting on wind rotors. As for hydrodynamic forces exerted on the floating platform, the calculation method combines potential flow theory and Morison's equation, so as to accurately capture inertial force and drag force effects simultaneously. The mooring system behavior is

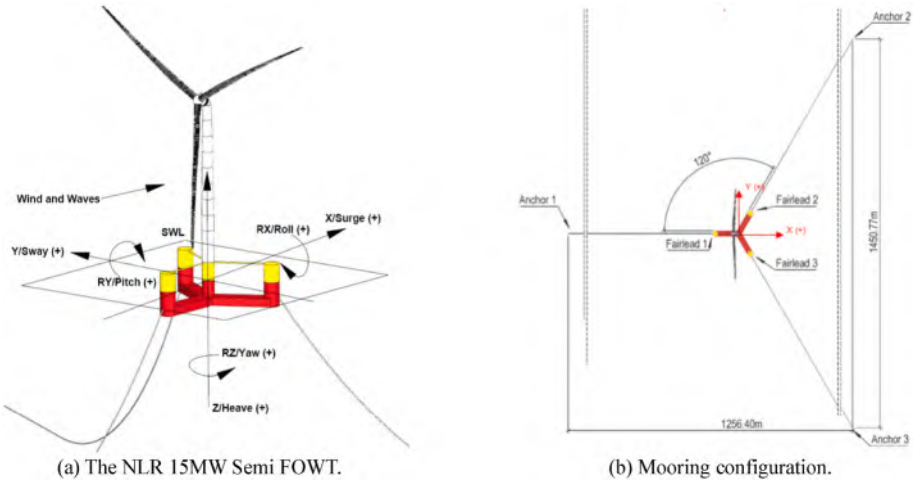

Fig. 9. Schematic of the FOWT and its mooring configuration (Allen et al., 2020).

solved by the embedded MoorDyn module in OpenFAST. This module divides mooring lines based on the lumped mass method, and adopts point mass and rigid body elements to fit various practical mooring layouts. Previous independent studies have fully verified the reliability of MoorDyn (Hall and Goupee, 2015), and users can check its complete technical specifications via the official document: https://moordyn.readthedocs.io/en/latest/. All dynamic responses of the floating wind turbine are solved through time-domain integration. The studied platform structure contains one central column for supporting wind turbine equipment and three peripheral columns connected by buoyancy pontoons and reinforcing braces. The whole mooring system is composed of three anchor cables arranged in a symmetrical pattern, with each cable fixed on one outer column at an angular interval of 120°.

All numerical simulations carried out in this work prescribe the wind, wave, and current directions as independent parameters, so that misaligned wind-wave-current conditions are explicitly included; the directional combinations adopted for each load case are summarized in Table 2. To reproduce real marine environmental characteristics, irregular sea waves are generated based on the JONSWAP spectrum (Mazzaretto et al., 2022). Meanwhile, the Kaimal spectrum is applied to establish full-scale turbulent wind fields, where the overall wind strength is determined by mean wind velocity. The specific formula of the JONSWAP random wave spectrum is presented below.

$$S(f)=\alpha\frac{H_s^2}{T_p^4 f^5}exp\left[-\frac{5}{4}(T_p f)^{-4}\right]\gamma^{exp\left[-\frac{(T_p f-1)}{2\sigma^2}\right]} \tag{15}$$

In the above formula, α refers to the Phillips constant, T_p denotes the peak wave period, and H_s represents the significant wave height. The variable f corresponds to the wave frequency, whereas γ is defined as the spectral shape parameter that controls the sharpness of the JONSWAP spectral distribution. The calculation criterion for the coefficient σ is specified in the equation below.

$$\sigma=\begin{cases}0.07, f\le f_p\\ 0.09, f>f_p\end{cases} \tag{16}$$

OpenFAST has gained extensive application in the dynamic response analysis of floating offshore wind turbines, with its reliability and computational accuracy fully verified via industrial practical validations (Robertson et al., 2017; Niranjan and Ramisetti, 2022; Wang et al., 2022a, b; Kim et al., 2025). The IEA 15 MW semi-submersible FOWT model adopted in this study is a canonical benchmark case widely recognized in the OpenFAST research community, and all its complete model resources are publicly available through the official IEA Wind Systems open-source repository (https://github.com/IEAWindSystems). Given that this study primarily focuses on the development and performance verification of NN models for FOWT mooring line tension prediction, detailed elaborations of turbine modeling schemes and numerical simulation procedures are omitted to maintain the conciseness of this paper. For comprehensive theoretical foundations, module principles and detailed simulation specifications of the OpenFAST software, readers may refer to its official technical documentation (https://openfast.readthedocs.io/en/main/index.html).

3.3. Definition of loading cases

This study focuses on the mooring tension responses of floating offshore wind turbines under parked operational conditions. Such scenarios are widely regarded as the most critical design-governing case for mooring systems, primarily because substantial current loads applied to the stationary platform can induce extreme mooring line tension. Accordingly, the environmental parameters corresponding to Load Case 6.1 from the official NLR 15 MW semi-submersible wind turbine report (Allen et al., 2020) are adopted to generate the simulation dataset in this work. Under the baseline wind, wave, and current conditions summarized in Table 1, a series of numerical simulations are conducted to investigate mooring tension variations under diverse environmental incident angles.

Table 1
Definition of load cases (LCs).

Load Cases	Inflow Wind	Wind Turbine	Hs	Tp	γ	Current
-	m/s		m	s	-	m/s
6.1	47.5	Parked	10.70	14.20	2.75	2.00

Table 2
Final composition of the testing dataset (✓: *Extrapolate TD*; ◯: *Interpolate TD*).

wdd	*wvd*	*crd*					
		0	60	120	180	240	300
0	**0**		◯		✓		
	60			◯	✓		
	120				✓		
	180	✓	✓	✓	✓	✓	✓
	240				✓		◯
	300	◯			✓		
60	**0**	◯			✓		
	60		◯		✓		
	120			◯	✓		
	180	✓	✓	✓	✓	✓	✓
	240				✓	◯	
	300				✓		◯
120	**0**				✓	◯	
	60				✓		
	120			◯	✓		
	180	✓	✓	✓	✓	✓	✓
	240	◯			✓		
	300		◯		✓		
180	**0**	✓	✓	✓	✓	✓	✓
	60	✓	✓	✓	✓	✓	✓
	120	✓	✓	✓	✓	✓	✓
	180	✓	✓	✓	✓	✓	✓
	240	✓	✓	✓	✓	✓	✓
	300	✓	✓	✓	✓	✓	✓

The parametric angle ranges are set as follows: wind direction (*wdd*) from 0° to 180° at 60° intervals, wave direction (*wvd*) from 0° to 180° at 60° intervals, and current direction (*crd*) from 0° to 300° at 60° intervals. All OpenFAST simulations run for a total duration of 3600 s, and the full time-history outputs, including the six-degree-of-freedom translational and rotational displacements of the floating platform and the tension time series of the three mooring lines, are presented in Fig. A-2 of Appendix Part I. For the convenience of result analysis and discussion in this study, environmental incident angles are divided into two categories based on their deviation from the negative *x*-axis. Angles with an absolute deviation smaller than 120° are defined as moderate wind-wave-current angles, while those exceeding 120° are classified as large wind-wave-current angles, and this customized classification is only used for unified reference throughout this paper. The geometric definition of these incident angles is visualized in Fig. 10. Furthermore, representative simulation results under typical wind, wave, and current directional conditions are supplemented in Fig. A-1 and Fig. A-2 of Appendix Part II.

4. Model training

4.1. Splitting of datasets

The full dataset covering all environmental incident angles (*wdd* = [0:180:60], *wvd* = [0:180:60], *crd* = [0:300:60]) is first categorized into two subsets with moderate and large *wind-wave-current* angles. The moderate angle group includes cases with *wdd*, *wvd* ranging from 0° to 120° at 60° intervals and *crd* ranging from −120° to 120° at 60° intervals, while all remaining cases are classified as the large-angle

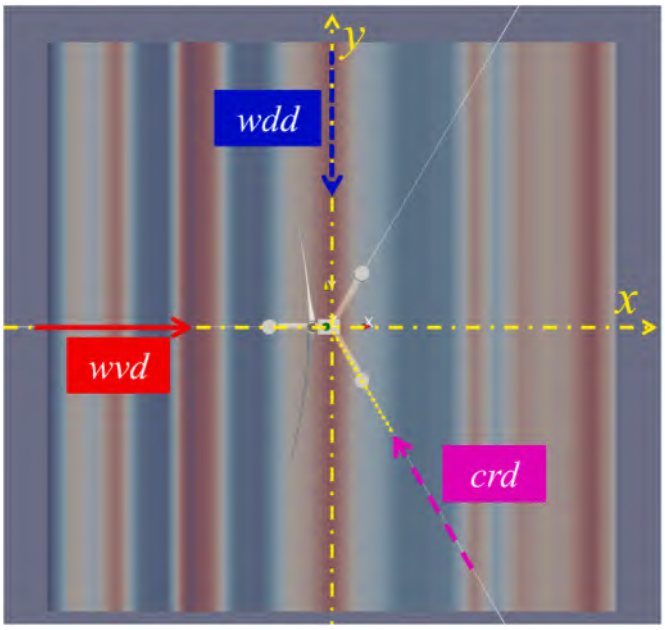

Fig. 10. Definition of wind-wave-current angles. The depicted loading condition corresponds to $wdd = 90$, $wvd = 0$, $crd = 240$.

group. All data from the large-angle group are reserved as the first part of the test dataset, named "*Extrapolation TD*". Since these environmental angles fall outside the range of the moderate-angle training domain, this test subset is adopted to quantitatively evaluate the extrapolation and generalization performance of the developed NN models.

The second test subset, termed "*Interpolation TD*", is randomly sampled from the moderate wind-wave-current angle dataset and excluded from model training. Although these samples are not involved in the training process, their corresponding environmental angles are distributed within the coverage of the training angle range. Therefore, this subset is used to examine the model's internal interpolation capability for unseen samples within the learned parameter space.

The third test dataset is defined as "*Time-Series TD*". For each load case adopted for model training, the last 25% of the full time-series data is retained and excluded from the training process. This unique test subset is designed to assess the model's accuracy and reliability in long-term time-series prediction tasks, focusing on its capability to capture temporal dynamic variations of mooring responses.

Collectively, the above three independent subsets constitute the entire test dataset, with all samples strictly excluded from model training to ensure unbiased performance evaluation. For the remaining available data, all input–output time-series pairs are fully shuffled to eliminate sequence bias. Subsequently, 80% of the shuffled data is selected as the training dataset, and the remaining 20% serves as the validation dataset for hyperparameter tuning and model optimization. The complete workflow of the dataset division strategy adopted in this study is illustrated in the corresponding figure below.

Detailed information regarding the final composition of the training and test datasets is presented in Table 2.

4.2. Training specifications

All NN models in this study are optimized using the root mean square error (E_{RMS}) loss function, whose mathematical expression is shown in Eq. (17).

$$E_{RMS} = \sqrt{\frac{1}{m}\sum_{i=1}^{m}\left(y_i - y_i^{pred}\right)^2} \tag{17}$$

In this study, the Rectified Linear Unit (*ReLU*) function, formulated in Eq. (18), is adopted as the activation function for the hidden layers of constructed NNs. As a simple piecewise-linear function, *ReLU* efficiently introduces nonlinear characteristics into the network, which is essential for fitting the complex nonlinear relationship inherent in FOWT mooring tension responses.

$$ReLU(x) = max(0, x) \tag{18}$$

All NN models in this work are developed, trained and validated based on the open-source PyTorch deep learning framework (Paszke et al., 2019). The Adamax optimization algorithm integrated in PyTorch is selected for model parameter updating, which is an improved variant of the conventional Adam optimizer (Kingma and Ba, 2017) that applies the infinity norm to constrain gradient magnitudes. This optimization strategy delivers more robust and faster convergence performance when handling datasets with noisy and sparse gradient features, which perfectly suits the fluctuating characteristics of mooring tension time-series data. To balance training convergence and generalization capability and avoid overfitting, an early stopping strategy is applied throughout the training process. The model training terminates automatically if the validation loss fails to decrease within 50 consecutive epochs, ensuring the optimized model achieves reliable generalization performance on unseen data.

The complete hyperparameter settings for all four NN models are summarized in Table 3 below. The input history length is fixed at 20 s, and the prediction lead time ranges from 5 s to 20 s.

5. Model evaluation and discussion

5.1. Statement of evaluation procedure

As illustrated in Fig. 11 and summarized in Table 2, three independent test datasets are established in this study, namely the *Time-Series TD*, *Interpolation TD*, and *Extrapolation TD*. Model evaluation is conducted separately on these three datasets to comprehensively examine the network performance from different perspectives. Among the three test groups, the *Time-Series TD* is derived from the same environmental load cases that are involved in model training. Specifically, this test subset consists of the last 25% of the complete time series extracted from

Table 3
Hyperparameter settings for all four NN models.

Hyperparameter	NN-1 GRU	NN-2 GRU-MHA	NN-3 Enc-Dec-Full	NN-4 Enc-Dec-Simplified
GRU layers	2	2	2 (encoder)	2 (encoder)
GRU hidden dimension	128	128	128	128
MLP layers (output head)	2	2	2	2
MLP hidden dimension	64	64	64	64
Number of attention heads	-	4	4	4
Attention dim (d_k/d_v)	-	32	32	32
Decoder MLP layers	-	-	2	2
Decoder hidden dimension	-	-	64	64
Positional embedding	-	-	Yes	No
Optimizer	Adamax	Adamax	Adamax	Adamax
Learning rate	1e-4	1e-4	1e-4	1e-4
Weight decay	1e-5	1e-5	1e-5	1e-5
Batch size	32	32	32	32
Maximum epochs	2000	2000	2000	2000
Early-stopping patience	50 epochs	50 epochs	50 epochs	50 epochs
Input history length	20 s	20 s	20 s	20 s
Prediction lead time	5–20 s	5–20 s	5–20 s	5–20 s
Sampling interval	0.5 s	0.5 s	0.5 s	0.5 s
Normalization method	min-max	min-max	min-max	min-max

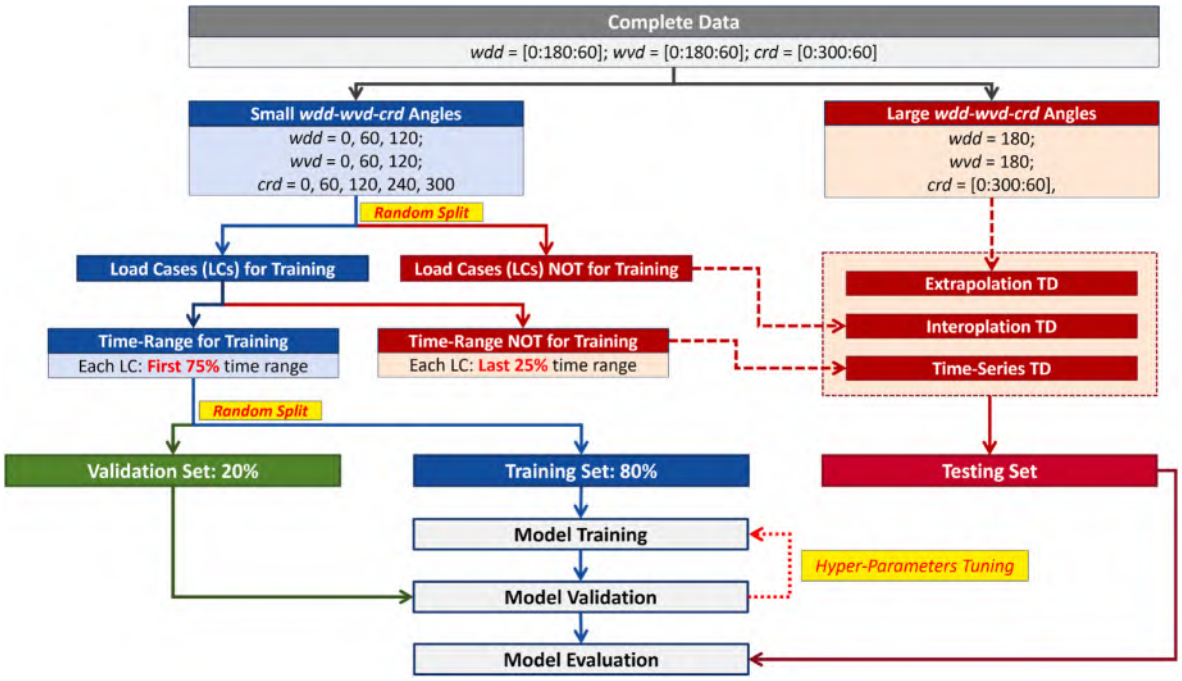

Fig. 11. Details of data-splitting.

each training load case, which is reserved exclusively for testing and excluded from the model training process.

Fig. 12 visualizes the data partitioning strategy based on the full mooring tension time series of a typical load case with unified wind, wave, and current directions ($wdd = 0$, $wvd = 0$, $crd = 0$). For each time series sample, the first 75% of the data (marked with a blue background) is assigned for model training, whereas the last 25% segment (marked with a red background) is retained for testing, corresponding to the proposed *Time-Series TD*. This evaluation strategy enables a systematic and multi-dimensional assessment of model performance through three progressive validation steps. The evaluation workflow starts with the *Time-Series TD* to verify the model's basic prediction accuracy under the environmental conditions covered by the training dataset. Next, the model is tested on the *Interpolation TD* to validate its interpolation capability, which reflects the model's adaptability to unseen samples within the range of trained wind, wave, and current angles. Finally, performance evaluation is conducted on the *Extrapolation TD* to assess the model's extrapolation ability for novel environmental load cases with directional conditions that are not included in the training data distribution.

To comprehensively and quantitatively assess the prediction performance of the developed NN models, two mainstream statistical evaluation metrics are adopted in this study. These quantitative indicators include the coefficient of determination (R^2-score) and Mean Absolute Percentage Error (MAPE), which jointly provide a comprehensive assessment of model fitting performance, numerical error magnitude, and overall prediction reliability. The definition of those metrics is provided by Eqs. (19) and (20).

$$R^2 = 1 - \frac{\sum_{i=1}^{N}\left(y_i - y_i^{pred}\right)^2}{\sum_{i=1}^{N}\left(y_i - \overline{y_i}\right)^2} \tag{19}$$

$$\mathrm{MAPE} = \frac{1}{N}\sum_{1}^{N}\left|\frac{y_i - y_i^{pred}}{y_i}\right| \times 100\% \tag{20}$$

In above equations, N refers to the total number of data samples, y_i stands for the reference value obtained from numerical simulations, $\overline{y_i}$ represents the average of all reference values, and y_i^{pred} corresponds to the model-predicted result. As a critical evaluation indicator, the R^2-score ranges from 0 to 1. A higher R^2-score closer to 1 signifies a better fitting effect and superior prediction accuracy, whereas a value closer to 0 indicates a weaker capability of the model to capture the inherent variation of mooring tension responses.

It should be further articulated here that mooring-line tension is given in kilonewtons (kN). Prior to computing the evaluation metrics, model predictions are denormalized to recover the physical (dimensional) tension values. Accordingly, all reported R^2-score and MAPE values are computed on the original kN-scale tension outputs.

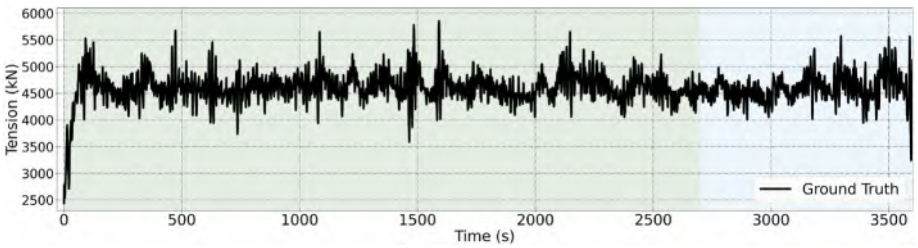

Fig. 12. Illustration of *Time-Series TD*. Training dataset: light-green background; *Time-Series TD*: light-blue background.

5.2. Evaluation of model performance under moderate wind-wave-current angles

5.2.1. Evaluation on training wind-wave-current angles

This study first evaluates the model prediction performance on the *Time-Series TD*, which is constructed from reserved test data under the identical wind-wave-current angle conditions used for model training. The specific data division strategy is demonstrated in Fig. 13. In this figure, the time-series segments with green backgrounds represent the data adopted for model training, while the segments with blue backgrounds are reserved independently for model testing. Three different prediction lead times are considered in this evaluation, which denote the time interval in advance of the current moment for NN prediction. For example, a lead time of 10 s indicates that the network predicts the mooring line tension 10 s after the current time step.

The setting of lead time (denoted by *Lead* in Fig. 13) is of great practical significance for the dynamic control of floating offshore wind turbines. Turbine control modules, such as blade pitch control and yaw control, cannot complete state adjustment instantaneously, and the platform itself can also be actuated, for example by transferring ballast water among the columns or by thruster-assisted station keeping. Therefore, predicting only the current tension state provides negligible guidance for real-time operational control. In contrast, reasonable lead time creates an effective time buffer for the control system to respond and adjust the platform or the turbine in advance. Furthermore, the prediction accuracy is found to increase with the reduction of lead time. This trend follows the inherent physical property of FOWT dynamic responses, where all motion-related time-series signals are continuous and differentiable over time, resulting in higher similarity between adjacent time steps.

The left column of Fig. 13 presents the overall prediction performance of the four proposed NN models on both the training dataset and the corresponding *Time-Series TD* from top to bottom, while the right column provides zoomed-in views of the prediction results on the *Time-Series TD*. For intuitive visualization and analysis, this figure only displays the typical training load case with identical environmental incident angles ($wdd = 0$, $wvd = 0$, $crd = 0$). Table 4 further quantifies the prediction accuracy of the four models under varying lead times for this specific load case. The statistical indicators including R^2-score and MAPE are calculated based solely on the *Time-Series TD* samples, corresponding to the blue-background time-series segments illustrated in Fig. 12.

Table 4
Comparison of R^2-scores of NN predictions on Training dataset (light-green background) and *Time-Series TD* (light-blue background) under the loading condition of $wdd = 0$, $wvd = 0$, $crd = 0$.

	NN-1	NN-2	NN-3	NN-4
Lead = 5s	0.969/0.964	0.970/0.969	0.930/0.923	0.955/0.951
Lead = 10s	0.921/0.911	0.933/0.930	0.911/0.907	0.940/0.929
Lead = 20s	0.722/0.710	0.795/0.788	0.855/0.839	0.865/0.845

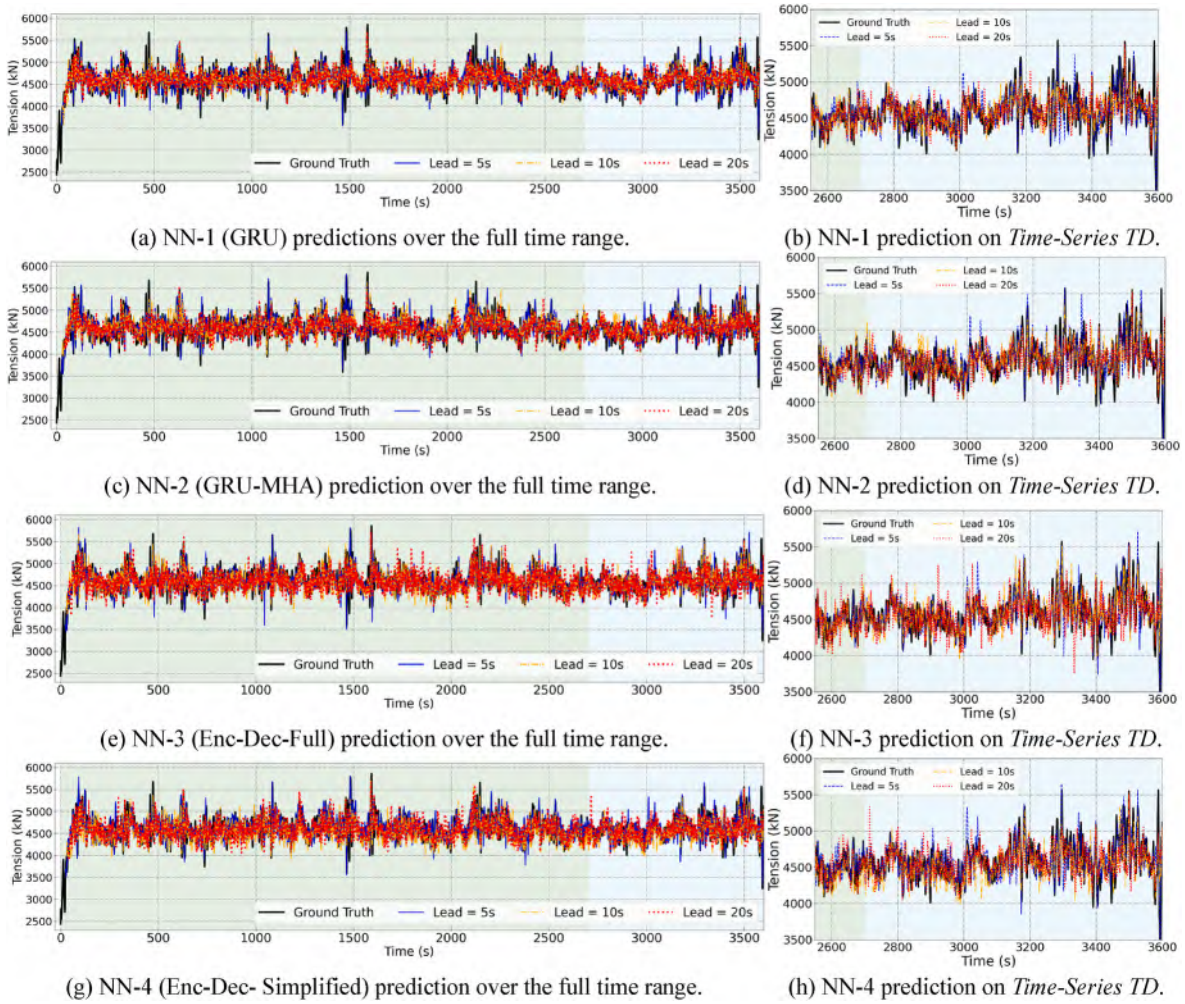

(a) NN-1 (GRU) predictions over the full time range.
(b) NN-1 prediction on *Time-Series TD*.
(c) NN-2 (GRU-MHA) prediction over the full time range.
(d) NN-2 prediction on *Time-Series TD*.
(e) NN-3 (Enc-Dec-Full) prediction over the full time range.
(f) NN-3 prediction on *Time-Series TD*.
(g) NN-4 (Enc-Dec- Simplified) prediction over the full time range.
(h) NN-4 prediction on *Time-Series TD*.

Fig. 13. Comparison of NN predictions for the loading condition of $wdd = 0$, $wvd = 0$, $crd = 0$ (within the range of wind-wave-current directions in the training dataset).

The prediction accuracy of all four NN models gradually declines as the lead time increases, which aligns with the expected variation trend. As mentioned earlier, the historical input length adopted for tension prediction is fixed at 20 s in this study, which is determined based on the authors' previous research and relevant references. Meanwhile, the JONSWAP wave spectrum applied for wave field generation has a peak period of 14.2 s. Given this parameter setting, the noticeable degradation in model performance with the lead time rising from 5 s to 10 s and 20 s is reasonable and predictable. Based on the above quantitative results, a lead time of 5 s is selected as the baseline condition for subsequent result analysis. It is worth noting that the core objective of this study is to validate the effectiveness of the proposed encoder-decoder network architecture. Therefore, the selection of lead time does not affect the core research conclusions of this work. A detailed discussion regarding the coupling relationship between lead time and historical input length can be found in the authors' previous studies (Ye et al., 2026).

In terms of the overall prediction performance of different network structures, NN-1 and NN-2 exhibit superior accuracy compared with NN-3 and NN-4, especially for NN-3. Specifically, the R^2-scores of the other three models on the *Time-Series TD* all exceed 0.95, while the accuracy of NN-3 is only approximately 0.92. The underlying reasons for such performance differences among the four models will be analyzed and discussed in detail in the subsequent sections. In general, the quantitative results demonstrate that for the wind-wave-current angle conditions used for model training, each NN model achieves comparable prediction accuracy on both the training time-series segments (green background) and the unseen test time-series segments (blue background). This consistent performance verifies that all models are well trained and meet the basic accuracy requirements for prediction tasks. Comprehensive quantitative evaluation results, including the R^2-score and MAPE values of the four NN models across all load cases, are summarized in Tables A-1 to A-4 of Appendix Part I. In these tables, cells with a white background correspond to the cases under training wind-wave-current angles, and all statistical values in these cells are calculated based on the *Time-Series TD* datasets.

5.2.2. Evaluation on interpolation TD

Fig. 14 presents the predictive performance of the four proposed NN models on the *Interpolation TD*, which consists of unseen load cases distributed within the parameter coverage of the training wind-wave-current angles. A typical interpolation case with the directional condition of $wdd = 60°$, $wvd = 120°$, and $crd = 120°$ is selected for graphical demonstration. In this figure layout, each row corresponds to one NN architecture from NN-1 to NN-4, while each column represents a specific prediction lead time, including 5 s, 10 s, and 20 s. Meanwhile, the relative absolute error (*RAE*, defined as $RAE = \left|\frac{y_i - y_i^{pred}}{y_i}\right| \times 100\%$, evaluated at

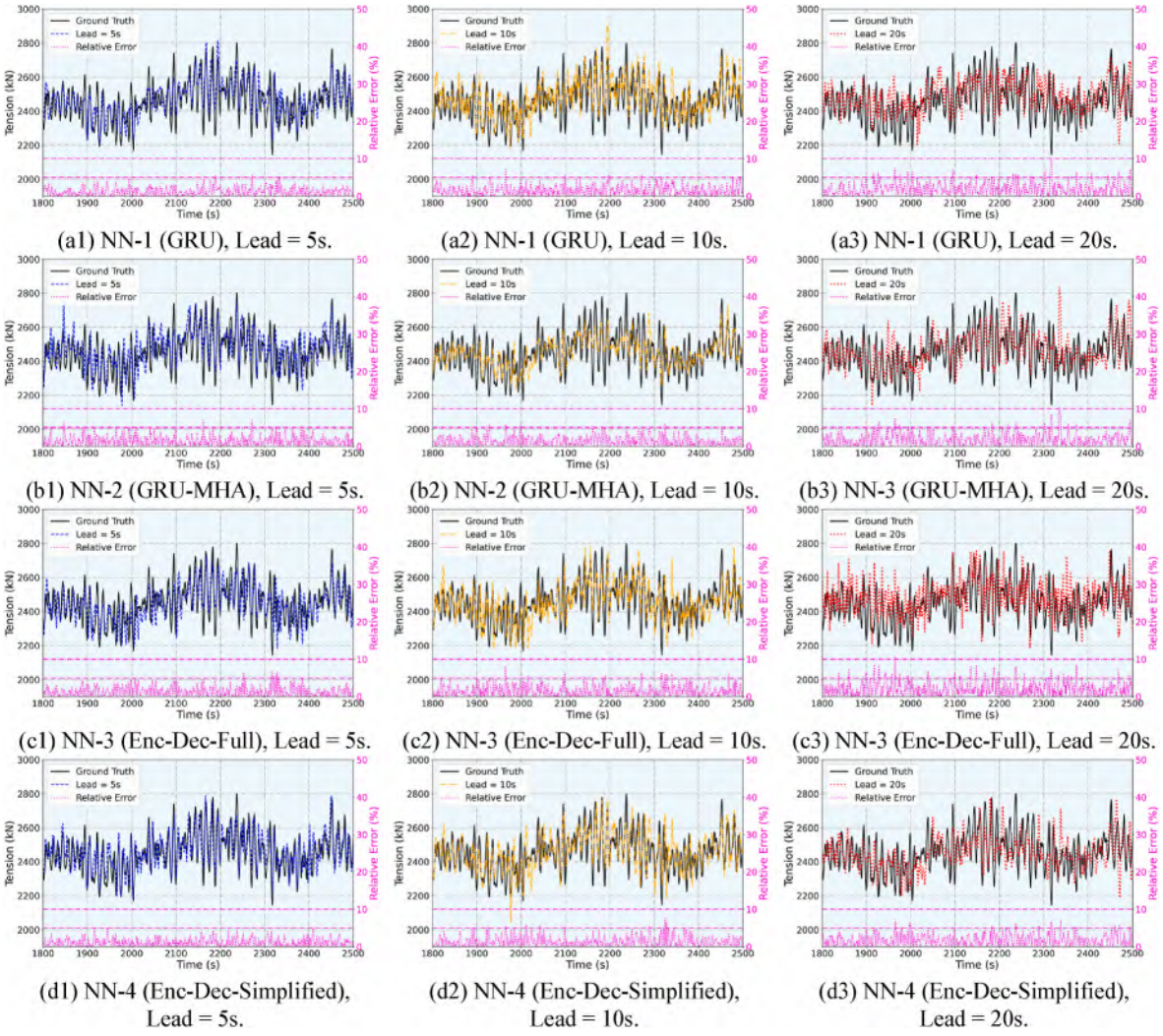

Fig. 14. Comparison of NN predictions for the loading condition of $wdd = 60$, $wvd = 120$, $crd = 120$. Note here that to be consistent with Figs. 11 and 12, light blue background is used to indicate that these datasets were not fed into the models in the training process.

each time instance) of each prediction result is plotted in magenta in every subfigure to provide an intuitive visual reference for the model prediction error.

As illustrated in Fig. 14, all adopted NN models achieve comparable prediction performance under the *Interpolation TD* dataset. This performance characteristic is reasonable and predictable, as the test conditions of *Interpolation TD* belong to the interpolation scenario. Although these working conditions are not included in the model training set, the corresponding wind, wave, and current angle ranges are fully covered by the training data distribution. According to the universal approximation theorem of neural networks, all NN architectures can theoretically fit the data distribution within the coverage range of the training set, thereby ensuring satisfactory prediction accuracy for interpolation tasks. This also explains that a sufficient and comprehensively covered dataset enables various NN models, as well as traditional linear interpolation methods, to obtain favorable prediction results. Nevertheless, actual engineering application scenarios often present distribution deviations between training data and practical operating conditions. For floating wind turbines, the wind-wave-current angles remain relatively stable during most operational periods, while extreme working conditions (e.g., typhoon conditions) can induce sudden large-angle deflection or even reverse changes in wind direction with the movement of typhoons. Such out-of-distribution working conditions are the key indicators for verifying the generalization and prediction accuracy of NN models, and the corresponding model performance evaluation under these scenarios will be elaborated in Section 5.3.

In addition, all four models exhibit a consistent error growth trend with the increase of lead time, which is consistent with the preliminary analysis in the previous sections. The prediction error remains below 5% when the lead time is no more than 10 s, but exceeds 10% when the lead time extends to 20 s, and this degradation tendency is also theoretically predictable. In this study, a unified 20-s time history is adopted for model input. Theoretically, accurate prediction for a longer lead time requires sufficient historical time-series data support. The influence of input history length and lead time on prediction accuracy has been demonstrated and discussed in our previous study, which also verified that excessively long time series do not continuously improve model performance. On the contrary, redundant time-series information may interfere with the model's capture of key physical features and obscure effective characteristic information, thus reducing prediction efficiency and accuracy. From a physical mechanism perspective rather than a pure data-driven view, accurate prediction of mooring line tension within a 20-s lead time requires richer long-term time-series feature information, especially considering that the peak wave period of the working conditions in this study is 14 s. Therefore, the significant decline in model prediction accuracy as the lead time increases from 10 s to 20 s is physically reasonable and consistent with the actual hydrodynamic variation characteristics of floating wind turbine systems.

Fig. 15 presents the corresponding frequency-domain results of the time-domain data illustrated in Fig. 14. All the established models can

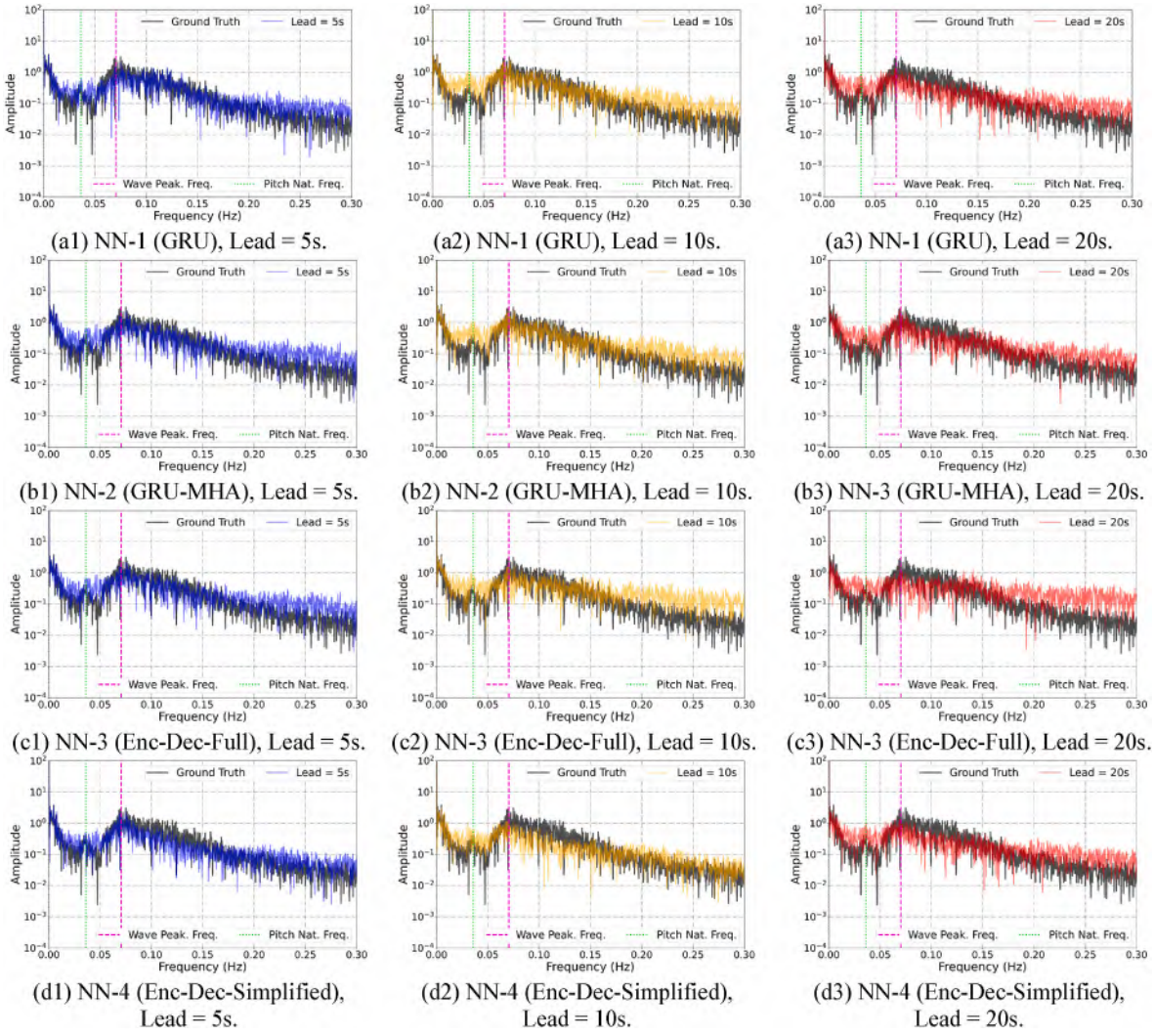

Fig. 15. Frequency-domain characteristics of NN predictions for the loading condition of $wdd = 60$, $wvd = 120$, $crd = 120$.

effectively capture the dominant wave frequency and the periodic characteristics of platform pitch motion. However, a common limitation is observed across all models: the prediction errors for high-frequency components are generally relatively large. Notably, the NN-4 model delivers outstanding prediction performance at a lead time of 5 s, achieving high accuracy for both low-frequency and high-frequency signal components. In addition, a clear degradation in spectral prediction accuracy can be observed for all models as the lead time increases, indicating that the model's ability to reproduce frequency-domain features gradually weakens with the extension of the prediction horizon.

Fig. 16 illustrates the scatter fitting accuracy of the four NN models on the *Interpolation TD*. Combined with the quantitative results listed in Tables A-1 to A-4 in Appendix Part I, it can be found that all models achieve good fitting performance on this interpolation test set, except for NN-3 (Enc-Dec-Full) which exhibits a relatively slightly lower accuracy with the overall R^2-score around 0.92. By comparison, the other three models yield competitive and satisfactory prediction accuracy, with their R^2-scores generally staying at approximately 0.96 and showing little performance discrepancy among one another.

5.2.3. Summary of model performance under moderate wind-wave-current angles

Fig. 17 summarizes the mooring tension prediction accuracy of the four NN models for test datasets within the wind-wave-current angle range covered by the training set, including the *Time-Series TD* and *Interpolation TD* defined previously. The corresponding detailed quantitative data can be referred to Tables A-1 to A-4 in *Appendix Part I*, in which the white-background and blue-background cells correspond to the *Time-Series TD* and *Interpolation TD* cases, respectively. In each subplot of Fig. 17, the solid red arrow represents the wind direction (*wdd*), and the dashed blue arrow denotes the wave direction (*wvd*). Each panel presents the prediction accuracy in terms of the R^2-score for FOWT mooring tension under the designated *wdd* and *wvd* conditions, across five different current directions (*crd*) of 0°, 60°, 120°, 240°, and 300°. In particular, the cases highlighted with a blue background correspond to the *Interpolation TD* samples that were not involved in the model training.

From Fig. 17, the following conclusions can be drawn intuitively.

1. The R^2-scores of all four models are higher than 0.92 under the presented moderate wind-wave-current conditions. Specifically, NN-1, NN-2 and NN-4 generally maintain R^2-scores above 0.95. Since the dataset is fully shuffled and all models are well trained, there is no substantial performance difference among various wind-wave-current angle cases.
2. The baseline GRU model achieves the most satisfactory prediction accuracy among the four models for working conditions within the wind-wave-current angle range of the training set. Meanwhile, the more advanced NN structures do not exhibit obvious performance improvements within the evaluated angle coverage of the test dataset.

5.3. Evaluation of model performance under large wind-wave-current angles (Extrapolation TD)

This section further examines the prediction accuracy of all models on the large wind-wave-current angle cases that are completely outside the parameter range of the training dataset, namely the *Extrapolation TD* defined in Fig. 9. Such evaluation effectively quantifies the generalization ability of the established NN models. Fig. 18 presents the time-series prediction results of the four NNs under the representative loading condition of *wdd* = 0°, *wvd* = 120°, and *crd* = 180°. Detailed quantitative data for all *Extrapolation TD* cases are summarized in Tables A-1 to A-4 of *Appendix Part I*.

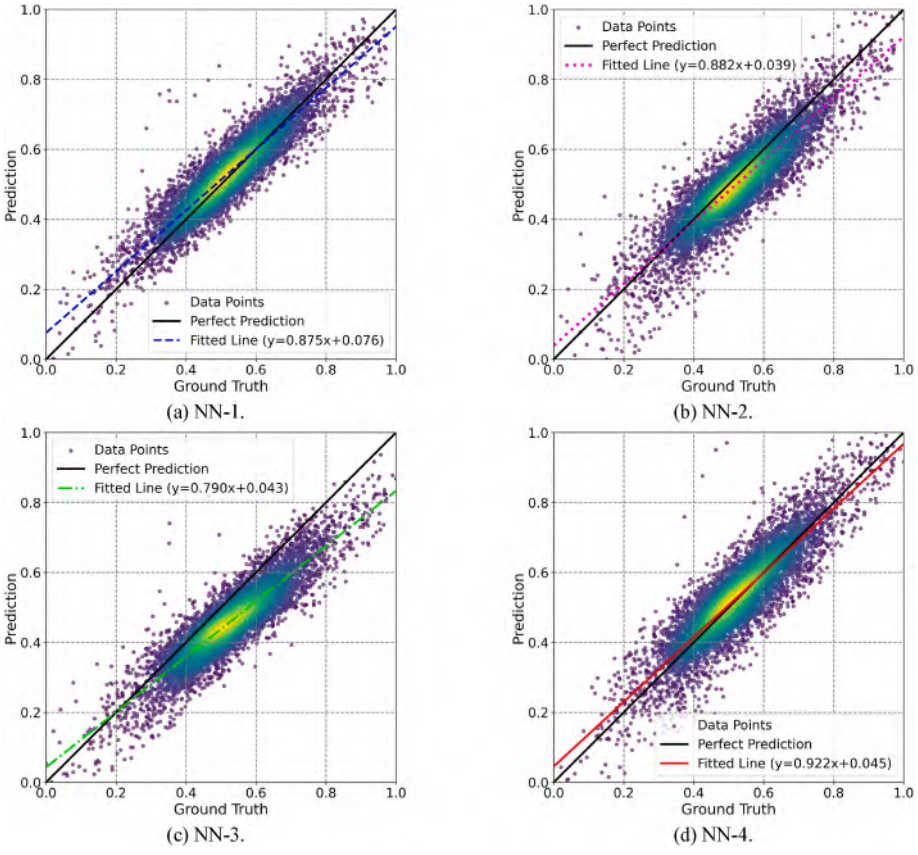

Fig. 16. Scatter fitting plot of predicted versus actual values on *Interpolation TD*.

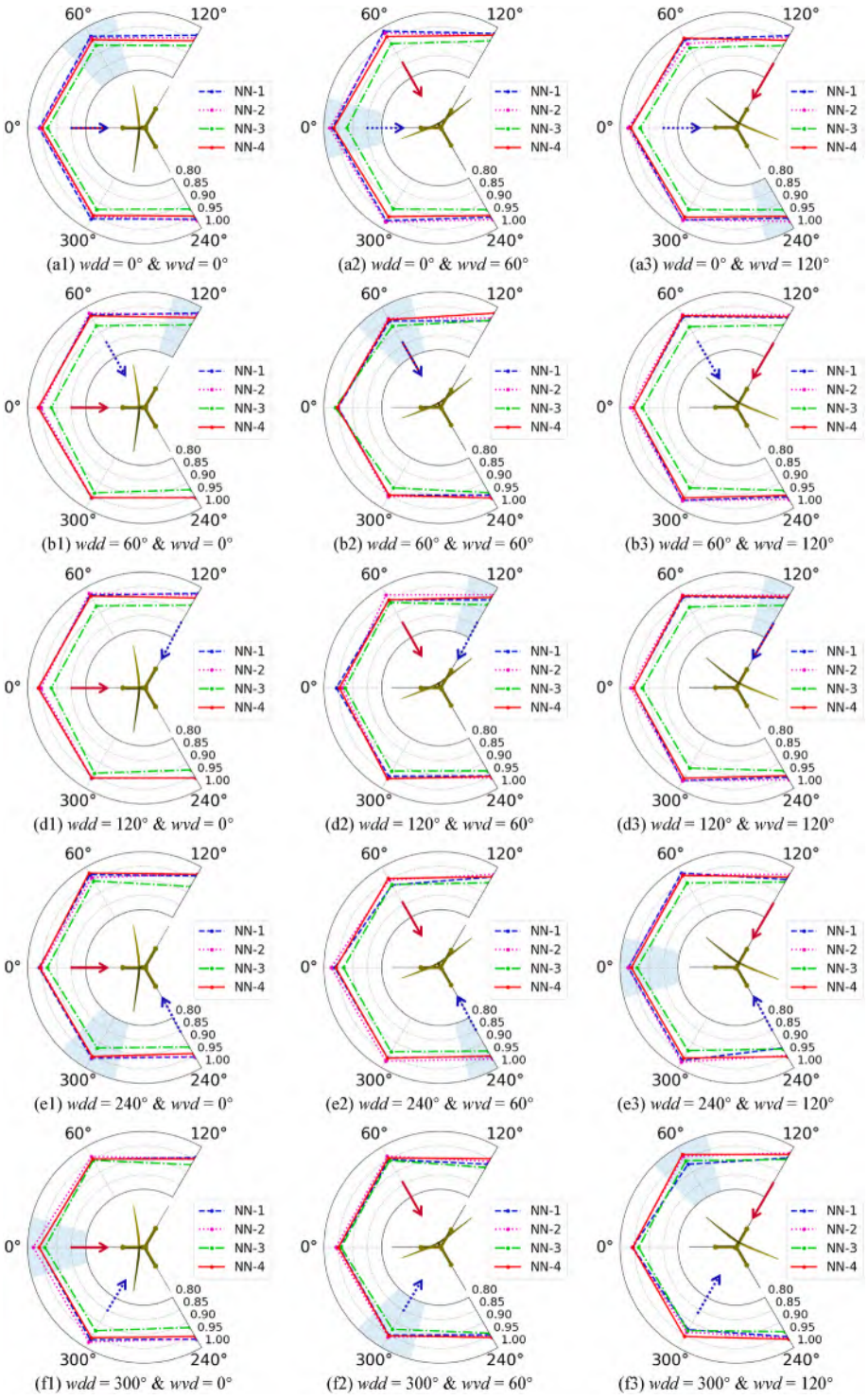

Fig. 17. Performance summary of four NN models under moderate wind-wave-current incident angles. A schematic top-view diagram of the FOWT is placed at the center of each panel. Solid red arrows indicate *wdd*, and dashed blue arrows denote *wvd*. Each panel shows the prediction accuracy (R^2) achieved by the models under specified *wdd* and *wvd* with different *crd*. Areas with blue background represent *Interpolation TD* cases that were not involved in model training, which is consistent with the notations used in previous figures.

The following conclusions can be drawn by observing the prediction results presented in Fig. 18.

1. NN-1 and NN-2, which achieved excellent performance on the *Interpolation TD* dataset, exhibit obvious prediction deviations under *Extrapolation TD* conditions. The mean values of mooring tension predicted by these two models are significantly lower than the ground truth. In terms of quantitative metrics including R^2-score and MAPE, their prediction accuracy declines remarkably from *Interpolation TD* to *Extrapolation TD*. This phenomenon indicates that NN-1 and NN-2 fail to effectively capture the directional characteristics of wind, wave and current loads.
2. By contrast, NN-3 and NN-4 can produce predicted mean values that agree well with the ground truth. Their R^2-score and MAPE values on

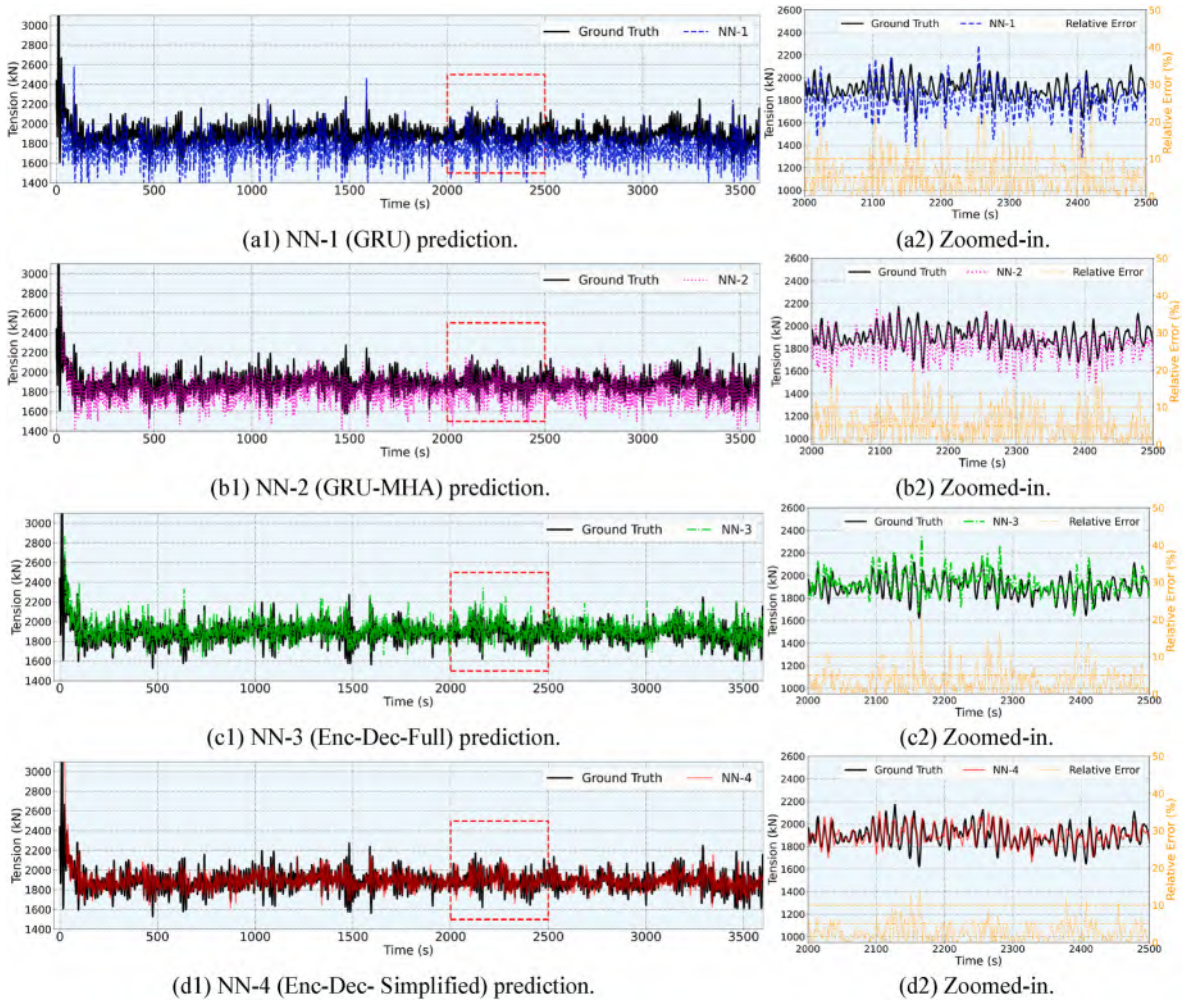

Fig. 18. Comparison of NN predictions for the loading condition of $wdd = 0$, $wvd = 120$, $crd = 180$. Note here that to be consistent with previous figures, light blue background is used to indicate that these datasets were not fed into the models in the training process.

Extrapolation TD remain at a similar level to those on *Interpolation TD*, without obvious accuracy degradation. It demonstrates that the encoder–decoder based NN-3 and NN-4 can effectively learn the inherent angular features of input environmental conditions.

3. Compared with NN-4, the time-series predictions of NN-3 show much stronger fluctuation characteristics. This can be further verified from Fig. 19, which presents the corresponding frequency-domain results of the time series in Fig. 18. By comparing Fig. 19(c) and (d), it is evident that NN-4 produces more reasonable spectral distributions, while NN-3 overestimates the high-frequency components of mooring tension responses.
4. The comparison between NN-3 and NN-4 clearly reveals that higher model complexity does not always lead to better prediction performance. The positional embedding module in the original Transformer architecture is designed to capture sequential dependencies for time-varying sequence information with distinct features at different positions. However, in the present study, the wind, wave and current directions remain fixed as static parameters under each individual load case. Imposing positional embedding on these invariant angular features unnecessarily increases model complexity, aggravates training difficulty, and brings no substantial improvement to prediction accuracy in the present dataset and model comparison. Instead, the simplified architecture of NN-4 achieves more reliable performance than the full-version NN-3 in the present dataset and model comparison. This finding suggests that when introducing advanced NN architectures from artificial intelligence into ocean engineering physical problems, researchers should fully consider the actual physical attributes of research objects, rather than unnecessarily increasing model complexity.

Fig. 20 displays the scatter fitting plots of predicted results against ground truth values for the four NNs on the *Extrapolation TD* dataset. Combined with the quantitative results summarized in Tables A–1 to A–4 in *Appendix Part I*, it can be observed that NN-1 and NN-2 deliver poor fitting performance, with their fitted curves showing obvious deviation from the ground truth distribution. This further confirms that the two baseline models cannot effectively capture the directional features of wind, wave and current angles. In contrast, NN-3 and NN-4 achieve a remarkable improvement in fitting accuracy, which demonstrates that the proposed encoder–decoder architectures are capable of effectively learning the angular characteristics of wind-wave-current misalignment.

5.4. Additional test of robustness to random initialization

Because the training of neural networks is sensitive to random weight initialization, the model comparison reported in the preceding

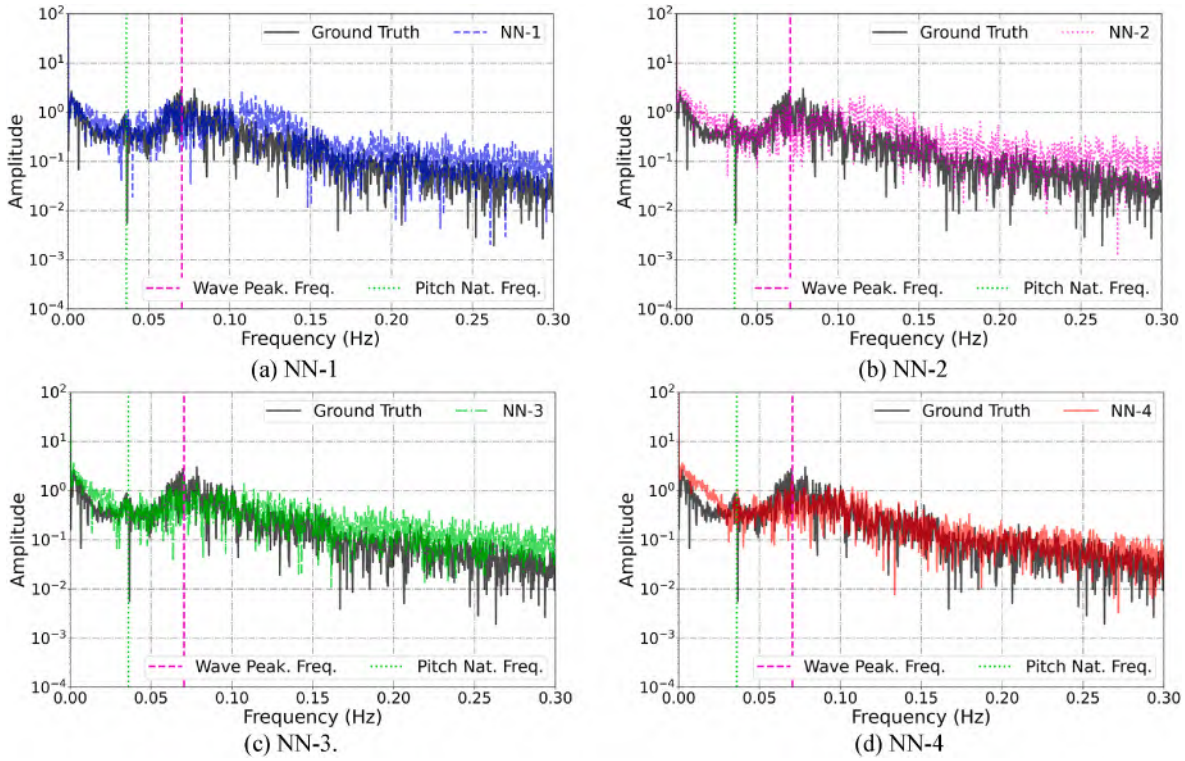

Fig. 19. Frequency-domain characteristics of NN predictions for the loading condition of $wdd = 0$, $wvd = 120$, $crd = 180$.

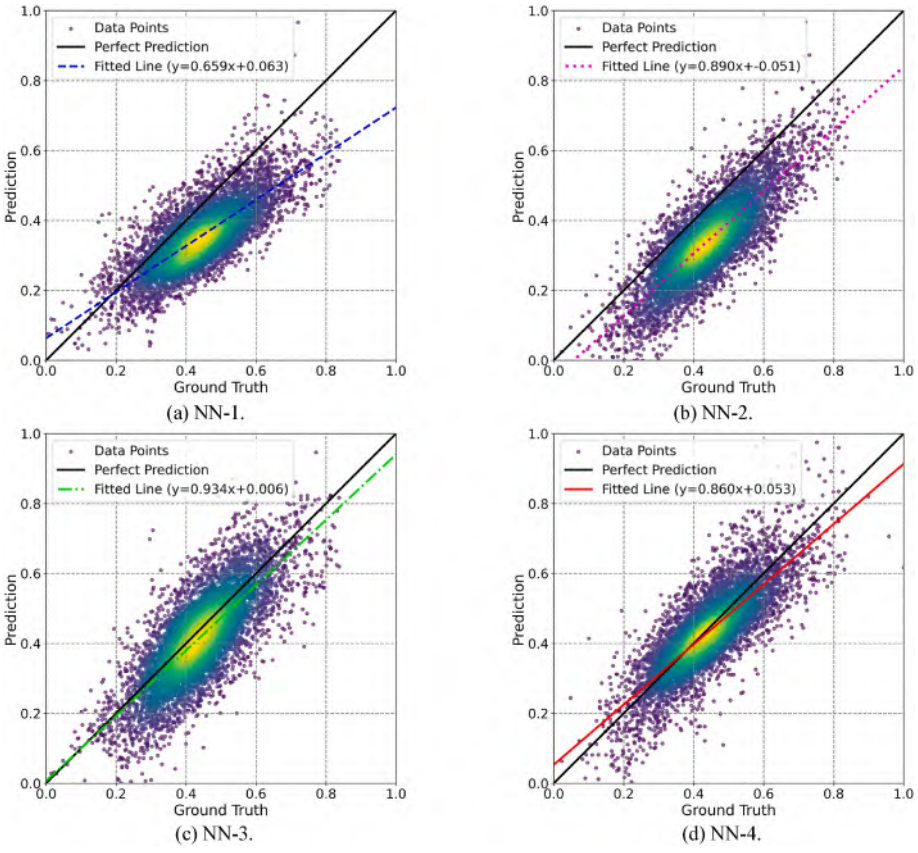

Fig. 20. Scatter fitting plot of predicted versus actual values on *Extrapolation TD*.

Table 5
Mean and standard deviation of the R^2-score and MAPE of the four NN models over 10 repeated training runs with different random seeds.

Model	Time-Series TD		Interpolation TD		Extrapolation TD	
	R^2-score	MAPE	R^2-score	MAPE	R^2-score	MAPE
NN-1 (GRU)	0.967 ± 0.004	2.9 ± 0.09	0.963 ± 0.006	3.1 ± 0.33	0.740 ± 0.007	7.8 ± 0.15
NN-2 (GRU-MHA)	0.972 ± 0.005	2.7 ± 0.08	0.967 ± 0.005	3.0 ± 0.31	0.804 ± 0.005	6.9 ± 0.13
NN-3 (Enc-Dec-Full)	0.923 ± 0.015	5.3 ± 0.19	0.922 ± 0.020	5.5 ± 0.61	0.901 ± 0.020	6.0 ± 0.46
NN-4 (Enc-Dec-Simplified)	0.956 ± 0.009	3.2 ± 0.15	0.955 ± 0.011	3.5 ± 0.36	0.928 ± 0.012	5.1 ± 0.32

subsections may be affected by the particular random seed adopted in each training run. To examine this effect, each of the four NN models was independently retrained 10 times with different random seeds, while all other training settings were kept identical to those described in Section 4.2. Randomness in the present training pipeline could in principle also arise from the mini-batch ordering, the dropout masks and the search over hyperparameters, whereas the train/validation/test partition is not a random quantity here, because the three test datasets are defined by the physically motivated ranges of wind, wave and current directions listed in Table 2. Isolating all of these sources and performing a complete variance decomposition would go beyond the scope of the present application-oriented study, and the check reported below therefore follows the common practice of varying the weight initialization alone while holding every other factor fixed. Ten repetitions were adopted as a compromise between statistical representativeness and computational cost: a larger number of runs would further reduce the statistical uncertainty of the reported means, but ten independent runs are sufficient to separate the systematic differences between the four architectures from the seed-to-seed scatter, while keeping the total training cost tractable with the computing resources available in this study. The mean and standard deviation of the R^2-score and MAPE over the 10 runs are summarized in Table 5 for the *Time-Series TD*, *Interpolation TD*, and *Extrapolation TD*.

The results in Table 5 show that the mean values of the four models are ordered exactly as in the single-run comparison reported in the preceding subsections, and that the differences between the mean values are larger than the corresponding standard deviations: the margin between NN-4 and NN-3 ranges from 0.027 to 0.033 in the R^2-score, whereas the standard deviation of NN-3 never exceeds 0.020, and the degradation of the two baseline models on the *Extrapolation TD* reaches 0.16-0.19 with a standard deviation of less than 0.01. This indicates that the performance differences reported above, in particular the comparison between NN-3 and NN-4, are determined by the network architecture rather than by random initialization, at least for the present dataset and model comparison. This empirical observation is consistent with the physical reasoning given in Section 2.3.4, where it was argued that positional embedding carries no additional information for the statically defined directional features; the repeated runs thus corroborate, rather than replace, the structural argument underlying the architecture comparison. Two features of the repeated runs nevertheless deserve a further comment. First, the run-to-run scatter is clearly structured: on all three test datasets and for both metrics it is largest for NN-3 (standard deviations of up to 0.020 in the R^2-score and 0.61 in the MAPE), intermediate for NN-4 (up to 0.012 and 0.36), and smallest for the two baseline models (at most 0.007 and 0.33). The two encoder-decoder variants are thus more sensitive to the weight initialization than the two simpler baselines, which is consistent with the larger number of trainable parameters that have to be determined from a limited engineering dataset. This does not, however, weaken the comparison between NN-3 and NN-4: the mean of NN-4 remains above that of NN-3 on all three test datasets, and the margin, although it narrows from 0.033 on the *Time-Series* and *Interpolation TDs* to 0.027 on the *Extrapolation TD*, remains larger than the standard deviation of either model. Second, the residual variability originates from the random weight initialization together with the stochastic components of the training procedure, namely the mini-batch ordering and the dropout masks, which act on a limited engineering dataset; because the loss surface of the present models is non-convex, different initializations may converge to different local minima that exhibit a comparable training loss but a slightly different generalization performance. Neither observation alters the main conclusion of the present study, namely that the positional embedding retained in NN-3 for the statically defined directional features brings no systematic gain in prediction accuracy, which confirms that an increase in model complexity does not necessarily improve the prediction performance in the present engineering problem. It should also be emphasized that this robustness check is restricted to a single reference FOWT, a single parked load case and ten repeated runs per model, and that the statistics reported in Table 5 refer to globally averaged metrics computed over the whole tension time series rather than to the extreme tension peaks that govern the safety of the mooring system; a dedicated analysis of the latter is left to ongoing work.

6. Conclusions

This study attempts to address the limitation of existing NN models for floating offshore wind turbine (FOWT) mooring tension prediction, where traditional models struggle to effectively capture inflow directional features of wind, wave and current. Inspired by the Transformer architecture widely adopted in natural language processing, this work proposes an encoder-decoder framework that takes wind-wave-current angle parameters as decoder inputs. The proposed architecture is validated using numerical simulation results of a reference 15 MW semi-submersible FOWT under parked condition with selected environmental loading directions. Under the dataset used in the present study, the proposed design enables the model to learn the directional characteristics of the environmental loads efficiently from a limited engineering dataset, thereby substantially improving its generalization to unseen directional combinations.

Four NN models of progressively increasing complexity are developed and compared in this work, namely a baseline GRU (NN-1), a GRU-MHA hybrid with concatenated directional inputs (NN-2), and the two Transformer-inspired encoder-decoder architectures proposed in this study, Enc-Dec-Full (NN-3) and Enc-Dec-Simplified (NN-4). The two encoder-decoder models share an identical dual-branch structure and differ only in whether positional embedding is applied to the directional features. Three independent test datasets, namely *Time-Series TD*, *Interpolation TD* and *Extrapolation TD*, are used for a step-by-step evaluation of the four models. The main conclusions are summarized as follows.

1. The baseline models NN-1 and NN-2 achieve satisfactory accuracy on *Interpolation TD*, within the wind-wave-current angle range covered by the training set, but degrade significantly on *Extrapolation TD* with unseen angular conditions. In contrast, the encoder-decoder models NN-3 and NN-4 maintain stable accuracy across both test sets and

outperform the baselines in generalization to out-of-distribution angular cases within the tested validation scope.
2. The improved performance of the encoder-decoder structures demonstrates their advantage in processing wind-wave-current directional information: attention is modelled separately for the temporal motion and thrust features in the encoder branch and for the static angular features in the decoder branch, and the cross-attention mechanism then fuses the global correlations between the two. This enables the model to learn the inherent directional characteristics of the environment and further enhances its generalization under unseen angular conditions.
3. This study also verifies that higher model complexity does not necessarily lead to better prediction performance. NN-3 inherits the positional embedding module from the original Transformer structure and imposes dynamic sequence encoding on static wind-wave-current angles. This operation introduces no valuable physical information, unnecessarily increases model complexity, and raises training difficulty without bringing any performance gain in the present dataset and model comparison. By removing the redundant positional embedding module, NN-4 achieves even better prediction results than NN-3 in the present dataset and model comparison. Taken together, these results suggest that when advanced NN architectures developed for artificial intelligence are transferred to ocean engineering problems, their physical relevance to the specific research object should be examined rather than assuming that additional structural complexity will improve the prediction; for the small-data engineering scenario considered here, simply enlarging the model is not a reliable route to higher accuracy.

Several limitations of the present study should be acknowledged, and each of them points to a natural direction for future work.

4. The numerical experiments are based on a single reference FOWT system under a single parked load case (the IEA 15 MW turbine on the UMaine VolturnUS-S semi-submersible platform under Load Case 6.1), so the conclusions are conditional on this particular turbine type and sea state. For the purpose of the present study, however, this configuration is sufficient, since the aim here is to propose and validate a new model architecture rather than to cover the full range of FOWT designs. Future work may explore a unified model that can handle different turbine types and different sea states.
5. The model is trained and evaluated on synthetic data generated by OpenFAST numerical simulations, and validation against field measurements is therefore lacking, which is a limitation shared by most existing studies of this kind. Acquiring real operational data from FOWTs is nevertheless challenging in practice, as the authors have learned from their own experience. On the one hand, such data usually belong to the operators and are regarded as commercially sensitive, and are therefore not publicly available; on the other hand, field measurements are considerably noisier than numerical simulation results and are of lower quality, so their use introduces additional data-cleaning difficulties. Future work will therefore attempt to obtain such measured data and to address these issues in earnest.
6. The models are evaluated with global metrics (the R^2-score and MAPE) over the complete tension time series, following the prevailing practice, but these quantify only the overall agreement and cannot guarantee that the extreme tension peaks that govern the mooring safety are captured accurately. The absolute error at the extreme values and the sign of the prediction error are therefore also of practical importance, and a model that slightly over-predicts the extremes may be more useful in practice than one that is globally more accurate but occasionally under-predicts a peak; an assessment of the extreme-value accuracy and signed errors, together with a strategy that directly targets the maximum tension expected within a future time window, is under development and will be reported separately.

CRediT authorship contribution statement

Maokun Ye: Writing – original draft, Visualization, Validation, Software, Methodology, Data curation, Conceptualization. **Zhengrong Song:** Resources, Methodology, Data curation. **Xichong Yu:** Resources, Investigation, Data curation. **Decheng Wan:** Writing – review & editing, Supervision, Software, Project administration, Funding acquisition, Conceptualization.

Data availability

The data that support the findings of this study are available from the corresponding author upon reasonable request.

Declaration of competing interest

The authors declare that they have no known competing financial interests or personal relationships that could have appeared to influence the work reported in this paper.

Acknowledgements

This work was supported by the National Key Research and Development Program of China (2025YFF0515701), to which the authors are most grateful.

Appendix

Part I: *NN predictions*

Table A-1
R^2-scores and MAPE values of different LCs obtained by NN-1 for the training set (white cells), *Interpolation TD* (blue cells), and *Extrapolation TD* (red cells).

		crd					
wdd	***wvd***	**0**	**60**	**120**	**180**	**240**	**300**
0	**0**	0.964/3.0%	0.963/2.9%	0.961/3.2%	0.823/7.7%	0.966/2.5%	0.970/2.3%
	60	0.966/2.4%	0.967/2.4%	0.951/3.5%	0.791/8.1%	0.971/2.2%	0.971/2.2%
	120	0.958/4.1%	0.960/3.8%	0.963/3.1%	0.755/8.7%	0.970/2.3%	0.977/2.0%
	180	0.766/8.4%	0.690/10.4%	0.434/11.5%	0.133/14.1%	0.411/11.2%	0.671/10.9%
	240	0.957/3.8%	0.961/3.4%	0.961/3.3%	0.725/9.0%	0.970/2.3%	0.965/3.0%
	300	0.967/2.4%	0.969/2.3%	0.961/3.4%	0.770/8.3%	0.951/4.5%	0.958/4.0%
60	**0**	0.956/3.6%	0.970/2.7%	0.971/2.9%	0.861/7.3%	0.986/1.7%	0.977/2.1%
	60	0.949/3.9%	0.950/3.8%	0.951/3.8%	0.813/8.1%	0.946/3.9%	0.946/3.8%
	120	0.951/3.8%	0.952/3.8%	0.957/3.7%	0.697/9.0%	0.951/3.8%	0.951/3.8%
	180	0.776/8.1%	0.500/11.2%	0.479/11.6%	0.201/14.0%	0.501/12.1%	0.521/12.0%
	240	0.955/3.8%	0.960/3.4%	0.963/3.3%	0.433/13.9%	0.929/5.3%	0.961/3.0%
	300	0.950/3.9%	0.951/3.8%	0.948/3.8%	0.673/9.3%	0.950/3.9%	0.931/4.1%
120	**0**	0.960/3.3%	0.967/2.9%	0.966/3.1%	0.881/7.0%	0.953/3.7%	0.969/2.6%
	60	0.956/3.7%	0.970/2.9%	0.953/3.7%	0.805/8.2%	0.963/3.5%	0.959/4.0%
	120	0.969/3.2%	0.970/3.1%	0.952/3.5%	0.693/9.0%	0.966/3.3%	0.966/3.4%
	180	0.810/8.2%	0.799/10.7%	0.656/12.9%	0.315/13.5%	0.691/12.8%	0.723/10.5%
	240	0.921/4.9%	0.971/3.1%	0.971/3.1%	0.729/9.0%	0.977/2.3%	0.951/3.9%
	300	0.957/3.4%	0.929/4.3%	0.956/3.8%	0.834/7.5%	0.931/4.5%	0.956/4.0%
180	**0**	0.633/10.2%	0.511/12.1%	0.503/12.3%	0.232/13.8%	0.478/12.6%	0.601/10.6%
	60	0.680/9.7%	0.610/10.5%	0.631/10.3%	0.310/13.4%	0.525/11.8%	0.533/11.6%
	120	0.523/11.9%	0.497/12.4%	0.455/12.9%	0.219/13.9%	0.477/12.7%	0.492/12.5%
	180	0.311/13.5%	0.323/13.3%	0.310/13.6%	0.297/13.7%	0.288/14.0%	0.288/14.0%
	240	0.423/13.0%	0.416/13.1%	0.399/13.2%	0.303/13.6%	0.430/12.9%	0.383/13.3%
	300	0.656/10.0%	0.660/9.8%	0.539/11.5%	0.158/14.2%	0.577/11.0%	0.352/13.4%

Table A-2
R^2-scores and MAPE values of different LCs obtained by NN-2 for the training set (white cells), *Interpolation TD* (blue cells), and *Extrapolation TD* (red cells).

		crd					
wdd	***wvd***	**0**	**60**	**120**	**180**	**240**	**300**
0	**0**	0.969/2.7%	0.953/4.0%	0.958/3.4%	0.843/7.2%	0.960/3.1%	0.959/3.1%
	60	0.970/2.4%	0.961/2.4%	0.961/3.5%	0.812/7.9%	0.959/2.2%	0.962/2.2%
	120	0.960/4.1%	0.958/3.8%	0.955/3.1%	0.761/6.6%	0.977/2.3%	0.970/2.0%
	180	0.760/8.3%	0.703/10.1%	0.545/11.8%	0.411/13.2%	0.451/12.7%	0.771/8.0%
	240	0.955/3.8%	0.959/3.4%	0.955/3.3%	0.730/8.8%	0.959/2.3%	0.972/3.0%
	300	0.965/2.4%	0.978/2.3%	0.981/1.9%	0.759/8.0%	0.961/4.5%	0.955/4.0%
60	**0**	0.965/2.4%	0.975/2.4%	0.980/2.0%	0.857/7.0%	0.979/2.2%	0.970/2.0%
	60	0.951/3.8%	0.955/3.5%	0.952/3.8%	0.820/7.8%	0.956/3.5%	0.956/3.6%
	120	0.958/3.7%	0.959/3.6%	0.937/4.5%	0.711/8.9%	0.971/2.8%	0.971/2.8%
	180	0.808/7.6%	0.612/10.9%	0.455/12.6%	0.423/13.1%	0.431/12.9%	0.613/10.7%
	240	0.965/2.4%	0.973/2.4%	0.975/2.1%	0.555/12.3%	0.949/2.9%	0.971/3.0%
	300	0.955/3.8%	0.958/3.5%	0.959/3.7%	0.701/9.1%	0.963/3.5%	0.942/3.7%
120	**0**	0.972/2.7%	0.967/2.9%	0.973/2.7%	0.901/6.5%	0.936/4.6%	0.963/2.6%
	60	0.966/3.2%	0.970/2.9%	0.963/3.2%	0.813/7.7%	0.970/2.9%	0.969/3.0%
	120	0.977/2.2%	0.979/2.2%	0.960/3.1%	0.701/9.0%	0.976/2.8%	0.977/2.7%
	180	0.841/7.1%	0.808/7.5%	0.677/10.2%	0.415/13.3%	0.659/10.5%	0.670/10.3%
	240	0.951/3.9%	0.977/2.5%	0.973/2.7%	0.699/9.2%	0.970/2.9%	0.971/3.1%
	300	0.962/3.4%	0.939/3.6%	0.959/3.6%	0.656/9.7%	0.963/3.5%	0.976/2.7%
180	**0**	0.702/10.4%	0.583/11.9%	0.574/12.2%	0.304/13.7%	0.550/12.4%	0.671/10.8%
	60	0.755/9.6%	0.681/10.6%	0.704/10.3%	0.384/13.3%	0.599/11.7%	0.606/11.5%
	120	0.596/11.8%	0.570/12.3%	0.528/12.8%	0.293/13.8%	0.551/12.5%	0.566/12.3%
	180	0.385/13.4%	0.396/13.2%	0.383/13.5%	0.371/13.6%	0.361/13.9%	0.362/13.9%
	240	0.496/12.9%	0.490/13.0%	0.473/13.1%	0.377/13.5%	0.504/12.8%	0.457/13.2%
	300	0.730/10.1%	0.733/9.9%	0.613/11.4%	0.232/14.1%	0.651/10.9%	0.426/13.3%

Table A-3
R^2-scores and MAPE values of different LCs obtained by NN-3 for the training set (white cells), *Interpolation TD* (blue cells), and *Extrapolation TD* (red cells).

		crd					
wdd	***wvd***	**0**	**60**	**120**	**180**	**240**	**300**
0	**0**	0.923/5.4%	0.925/5.5%	0.932/4.1%	0.901/5.9%	0.930/4.2%	0.929/4.7%
	60	0.925/5.5%	0.941/2.4%	0.922/3.5%	0.877/6.3%	0.920/2.2%	0.942/2.2%
	120	0.927/5.1%	0.940/3.8%	0.919/3.1%	0.873/5.7%	0.927/2.3%	0.930/2.0%
	180	0.891/6.4%	0.865/7.2%	0.889/6.7%	0.879/6.9%	0.863/7.5%	0.880/6.6%
	240	0.917/5.8%	0.921/3.4%	0.933/3.3%	0.891/6.1%	0.945/2.3%	0.923/3.0%
	300	0.920/5.4%	0.933/2.3%	0.941/3.4%	0.910/5.5%	0.947/4.5%	0.929/5.0%
60	**0**	0.926/6.6%	0.923/4.9%	0.921/4.9%	0.885/6.2%	0.936/4.1%	0.947/4.2%
	60	0.939/4.3%	0.920/5.8%	0.961/2.8%	0.875/6.5%	0.926/6.6%	0.948/3.7%
	120	0.931/3.5%	0.932/3.5%	0.927/3.3%	0.913/5.3%	0.941/3.9%	0.931/3.5%
	180	0.898/6.0%	0.906/5.6%	0.899/6.2%	0.870/7.3%	0.885/6.8%	0.888/6.5%
	240	0.933/3.8%	0.936/3.4%	0.933/3.7%	0.893/6.0%	0.931/4.0%	0.938/3.8%
	300	0.943/4.3%	0.927/5.7%	0.941/3.8%	0.916/5.2%	0.946/3.5%	0.918/5.7%
120	**0**	0.926/5.3%	0.926/5.4%	0.931/3.5%	0.900/6.0%	0.920/5.3%	0.929/3.9%
	60	0.930/4.7%	0.920/4.9%	0.923/4.7%	0.876/6.4%	0.923/4.5%	0.929/4.1%
	120	0.941/4.6%	0.943/4.7%	0.932/3.5%	0.919/5.1%	0.946/3.6%	0.951/3.4%
	180	0.918/5.0%	0.921/4.8%	0.900/5.8%	0.903/5.6%	0.916/5.2%	0.925/4.7%
	240	0.925/5.4%	0.931/4.1%	0.941/3.5%	0.911/5.4%	0.937/3.7%	0.941/4.5%
	300	0.937/4.4%	0.933/4.5%	0.936/4.1%	0.926/4.9%	0.945/3.5%	0.950/3.5%
180	**0**	0.832/8.1%	0.812/8.8%	0.831/8.2%	0.823/8.5%	0.833/8.0%	0.838/7.7%
	60	0.830/8.3%	0.818/8.6%	0.828/8.4%	0.821/8.6%	0.820/8.7%	0.821/8.5%
	120	0.841/7.6%	0.838/7.8%	0.809/9.0%	0.826/8.4%	0.810/8.9%	0.825/8.3%
	180	0.833/8.0%	0.831/8.2%	0.830/8.2%	0.830/8.1%	0.818/8.7%	0.822/8.5%
	240	0.840/7.7%	0.834/8.0%	0.840/7.6%	0.839/7.8%	0.823/8.4%	0.830/8.1%
	300	0.834/7.9%	0.829/8.2%	0.831/8.1%	0.820/8.8%	0.821/8.6%	0.826/8.3%

Table A-4
R^2-scores and MAPE values of different LCs obtained by NN-4 for the training set (white cells), *Interpolation TD* (blue cells), and *Extrapolation TD* (red cells).

		crd					
wdd	***wvd***	**0**	**60**	**120**	**180**	**240**	**300**
0	**0**	0.951/3.2%	0.949/3.4%	0.951/3.2%	0.916/4.8%	0.952/3.1%	0.948/3.1%
	60	0.962/2.4%	0.970/2.4%	0.963/3.5%	0.921/4.5%	0.956/2.2%	0.943/2.2%
	120	0.959/4.1%	0.959/3.8%	0.964/3.1%	0.921/5.3%	0.966/2.3%	0.959/2.0%
	180	0.918/5.0%	0.925/4.6%	0.929/4.3%	0.922/4.7%	0.913/5.2%	0.930/4.2%
	240	0.943/3.8%	0.955/3.4%	0.959/3.3%	0.931/4.1%	0.977/2.3%	0.972/3.0%
	300	0.956/2.4%	0.961/2.3%	0.961/3.4%	0.933/4.0%	0.952/4.5%	0.952/4.0%
60	**0**	0.949/3.6%	0.954/2.9%	0.966/2.9%	0.930/4.4%	0.965/1.7%	0.970/2.8%
	60	0.961/3.1%	0.949/3.5%	0.954/2.8%	0.922/4.6%	0.951/3.7%	0.977/2.3%
	120	0.953/3.8%	0.962/2.8%	0.947/3.4%	0.919/4.9%	0.951/3.7%	0.961/2.8%
	180	0.921/4.7%	0.916/5.1%	0.919/4.9%	0.900/5.6%	0.905/5.4%	0.928/4.4%
	240	0.953/3.8%	0.961/2.8%	0.959/2.8%	0.903/5.5%	0.955/3.0%	0.962/2.8%
	300	0.960/3.1%	0.953/3.5%	0.950/2.8%	0.926/4.5%	0.956/3.6%	0.953/3.3%
120	**0**	0.953/3.6%	0.956/2.9%	0.963/3.2%	0.927/4.3%	0.958/3.0%	0.950/3.8%
	60	0.950/3.6%	0.960/3.0%	0.953/3.7%	0.926/4.4%	0.967/3.4%	0.962/3.6%
	120	0.962/3.1%	0.970/3.1%	0.957/3.0%	0.930/4.2%	0.976/2.8%	0.951/3.9%
	180	0.920/4.8%	0.933/4.0%	0.922/4.6%	0.921/4.7%	0.923/4.5%	0.929/4.1%
	240	0.955/3.4%	0.961/3.1%	0.961/3.0%	0.921/4.7%	0.967/3.3%	0.961/3.5%
	300	0.967/3.0%	0.956/3.0%	0.956/3.8%	0.927/4.3%	0.970/3.0%	0.970/3.1%
180	**0**	0.854/7.1%	0.834/7.6%	0.852/7.2%	0.845/7.4%	0.855/7.0%	0.860/6.8%
	60	0.851/7.3%	0.840/7.5%	0.849/7.2%	0.842/7.5%	0.841/7.6%	0.843/7.4%
	120	0.862/6.7%	0.859/6.9%	0.830/7.8%	0.847/7.3%	0.831/7.7%	0.846/7.2%
	180	0.854/7.0%	0.852/7.1%	0.851/7.1%	0.850/7.2%	0.839/7.6%	0.843/7.4%
	240	0.861/6.8%	0.855/7.0%	0.861/6.7%	0.860/6.9%	0.844/7.3%	0.851/7.1%
	300	0.855/6.9%	0.850/7.2%	0.852/7.0%	0.841/7.7%	0.842/7.5%	0.847/7.3%

Part II: *OpenFAST simulation results*

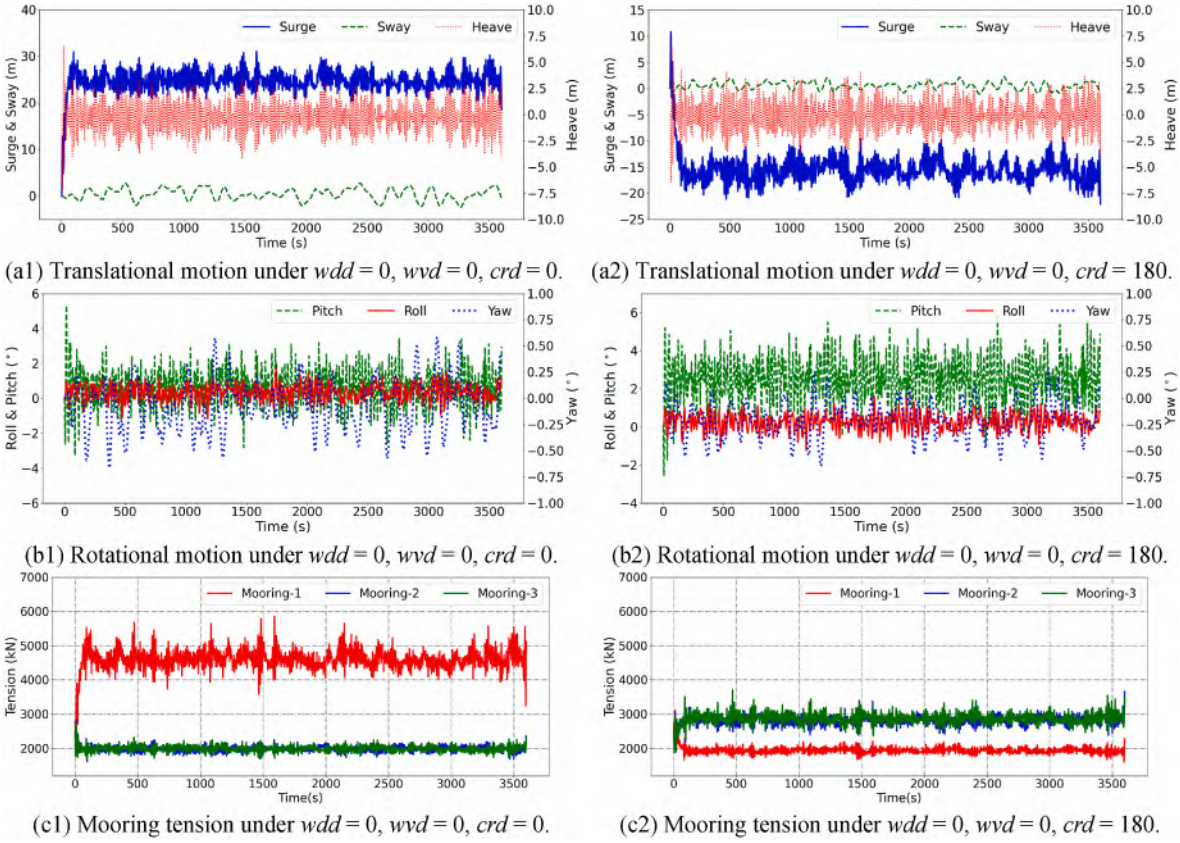

Fig. A-1. Numerical results of OpenFAST simulations.

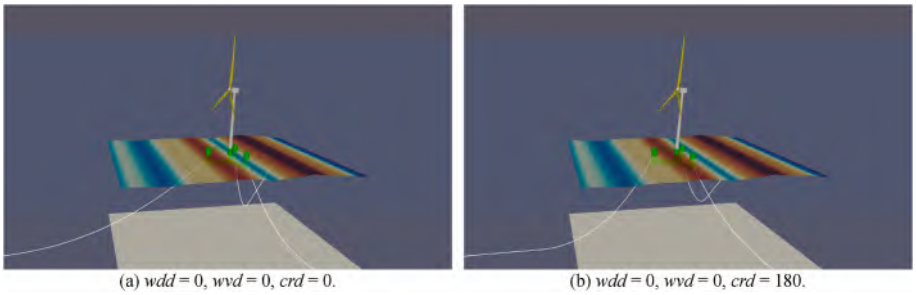

Fig. A-2. Visualization of simulation results at the time instant of 300 s.

Appendix A. Supplementary data

Supplementary data to this article can be found online at https://doi.org/10.1016/j.oceaneng.2026.129184.

References

Allen, C., Viscelli, A., Dagher, H., Goupee, A., Gaertner, E., Abbas, N., Hall, M., Barter, G., 2020. Definition of the UMaine VolturnUS-S reference platform developed for the IEA wind 15-Megawatt offshore reference wind turbine. https://doi.org/10.2172/1660012.

Chen, H., Bu, Y., Zong, K., Huang, L., Hao, W., 2022. The effect of data skewness on the LSTM-based mooring load prediction model. J. Mar. Sci. Eng. 10, 1931. https://doi.org/10.3390/jmse10121931.

Chen, Y., Yuan, L., Zan, Y., Li, Z., 2025. Forecasting mooring tension of offshore platforms based on complete ensemble empirical mode decomposition with adaptive noise and deep learning network. Measurement 239, 115515. https://doi.org/10.1016/j.measurement.2024.115515.

Chung, J., Gulcehre, C., Cho, K., Bengio, Y., 2014a. Empirical Evaluation of Gated Recurrent Neural Networks on Sequence Modeling.

Chung, J., Gulcehre, C., Cho, K., Bengio, Y., 2014b. Empirical evaluation of gated recurrent neural networks on sequence modeling. https://doi.org/10.48550/arXiv.1412.3555.

Deng, S., Ning, D., Mayon, R., 2024. The motion forecasting study of floating offshore wind turbine using self-attention long short-term memory method. Ocean. Eng. 310, 118709. https://doi.org/10.1016/j.oceaneng.2024.118709.

Gaertner E, Rinker J, Sethuraman L, Zahle F, Anderson B, Barter G, Abbas N, Meng F, Bortolotti P, Skrzypinski W, Scott G, Feil R, Bredmose H, Dykes K, Shields M, Allen C, Viselli A. Definition of the IEA 15-Megawatt Offshore Reference Wind Turbine n.d.

Gong, Z., Wan, A., Ji, Y., AL-Bukhaiti, K., Yao, Z., 2024. Improving short-term offshore wind speed forecast accuracy using a VMD-PE-FCGRU hybrid model. Energy 295, 131016. https://doi.org/10.1016/j.energy.2024.131016.

Gu, H., Chen, H.-C., 2024a. Numerical simulation of a semi-submersible FOWT platform under calibrated extreme and irregular waves. Ocean. Eng. 311, 118847. https://doi.org/10.1016/j.oceaneng.2024.118847.

Gu, H., Chen, H.-C., 2024b. Verification and validation of a coupled CFD–FEM approach with overset structured grid through free decay and regular wave tests. Appl. Ocean Res. 150, 104126. https://doi.org/10.1016/j.apor.2024.104126.
Halder, R., Damodaran, M., Khoo, B.C., 2023. Deep learning-driven nonlinear reduced-order models for predicting wave-structure interaction. Ocean. Eng. 280, 114511. https://doi.org/10.1016/j.oceaneng.2023.114511.
Hall, M., Goupee, A., 2015. Validation of a lumped-mass mooring line model with DeepCwind semisubmersible model test data. Ocean. Eng. 104, 590–603. https://doi.org/10.1016/j.oceaneng.2015.05.035.
He, K., Zhang, X., Ren, S., Sun, J., 2015. Deep Residual Learning for Image Recognition. https://doi.org/10.48550/arXiv.1512.03385.
Hu, L., Shi, W., Hu, W., Chai, W., Hu, Z., Wu, J., Li, X., 2025. Short-term prediction of mooring tension for floating offshore wind turbines under typhoon conditions based on the VMD-MI-LSTM method. Renew. Sustain. Energy Rev. 216, 115606. https://doi.org/10.1016/j.rser.2025.115606.
Jin, X., Dai, C., Tao, Y., Zhang, F., 2025. A comparative study of RNN, CNN, LSTM and GRU for random sea wave forecasting. Ocean. Eng. 338, 122013. https://doi.org/10.1016/j.oceaneng.2025.122013.
Jonkman, J.M., 2007. Dynamics modeling and loads analysis of an offshore floating wind turbine.
Kim, Y.J., Charlou, M., Bouscasse, B., Leroy, V., Aliyar, S., Bonnefoy, F., Kim, K.-H., Choi, Y.-M., 2025. High fidelity simulations of a floating offshore wind turbine in irregular waves by coupling OpenFOAM and OpenFAST. Renew. Energy 243, 122486. https://doi.org/10.1016/j.renene.2025.122486.
Kingma, D.P., Ba, J., 2017. Adam: a method for stochastic optimization. https://doi.org/10.48550/arXiv.1412.6980.
Lee, H., Ahn, Y., 2025. Comparative study of RNN-based deep learning models for practical 6-DOF ship motion prediction. J. Mar. Sci. Eng. 13, 1792. https://doi.org/10.3390/jmse13091792.
Li, Y., Xiao, L., Wei, H., Li, D., Li, X., 2025. A comparative study of LSTM and temporal convolutional network models for semisubmersible platform wave runup prediction. J. Offshore Mech. Arctic Eng. 147, 011202. https://doi.org/10.1115/1.4063266.
Ma, G., Jiang, H., Chen, H., Sun, K., Zhang, J., Yang, H., 2026. Prediction of FOWT mooring tension during non-stationary typhoon transit: a transformer based framework with Bayesian optimization. Ocean. Eng. 353, 124758. https://doi.org/10.1016/j.oceaneng.2026.124758.
Mazzaretto, O.M., Menéndez, M., Lobeto, H., 2022. A global evaluation of the JONSWAP spectra suitability on coastal areas. Ocean. Eng. 266, 112756. https://doi.org/10.1016/j.oceaneng.2022.112756.
Niranjan, R., Ramisetti, S.B., 2022. Insights from detailed numerical investigation of 15 MW offshore semi-submersible wind turbine using aero-hydro-servo-elastic code. Ocean. Eng. 251, 111024. https://doi.org/10.1016/j.oceaneng.2022.111024.
Paszke, A., Gross, S., Massa, F., Lerer, A., Bradbury, J., Chanan, G., Killeen, T., Lin, Z., Gimelshein, N., Antiga, L., Desmaison, A., Kopf, A., Yang, E., DeVito, Z., Raison, M., Tejani, A., Chilamkurthy, S., Steiner, B., Fang, L., Bai, J., Chintala, S., 2019. PyTorch: an Imperative Style, High-Performance Deep Learning Library.
Payenda, M.A., Wang, S., Jiang, Z., Prinz, A., 2024. Prediction of mooring dynamics for a semi-submersible floating wind turbine with recurrent neural network models. Ocean. Eng. 313, 119490. https://doi.org/10.1016/j.oceaneng.2024.119490.
Qiao, D., Li, P., Ma, G., Qi, X., Yan, J., Ning, D., Li, B., 2021. Realtime prediction of dynamic mooring lines responses with LSTM neural network model. Ocean. Eng. 219, 108368. https://doi.org/10.1016/j.oceaneng.2020.108368.
Rinker, J., Gaertner, E., Zahle, F., Skrzypiński, W., Abbas, N., Bredmose, H., Barter, G., Dykes, K., 2020. Comparison of loads from HAWC2 and OpenFAST for the IEA wind 15 MW reference wind turbine. J. Phys., Conf. Ser. 1618, 052052. https://doi.org/10.1088/1742-6596/1618/5/052052.
Robertson, A.N., Wendt, F., Jonkman, J.M., Popko, W., Dagher, H., Gueydon, S., Qvist, J., Vittori, F., Azcona, J., Uzunoglu, E., Soares, C.G., Harries, R., Yde, A., Galinos, C., Hermans, K., De Vaal, J.B., Bozonnet, P., Bouy, L., Bayati, I., Bergua, R., Galvan, J., Mendikoa, I., Sanchez, C.B., Shin, H., Oh, S., Molins, C., Debruyne, Y., 2017. OC5 project phase II: validation of global loads of the DeepCwind floating semisubmersible wind turbine. Energy Proc. 137, 38–57. https://doi.org/10.1016/j.egypro.2017.10.333.
Sherstinsky, A., 2020. Fundamentals of recurrent neural network (RNN) and long short-term memory (LSTM) network. Phys. Nonlinear Phenom. 404, 132306. https://doi.org/10.1016/j.physd.2019.132306.
Shi, W., Hu, L., Lin, Z., Zhang, L., Wu, J., Chai, W., 2023. Short-term motion prediction of floating offshore wind turbine based on muti-input LSTM neural network. Ocean. Eng. 280, 114558. https://doi.org/10.1016/j.oceaneng.2023.114558.
Song, B., Zhou, Q., Chang, R., 2025. Short-term motion prediction of FOWT based on time-frequency feature fusion LSTM combined with signal decomposition methods. Ocean. Eng. 317, 120046. https://doi.org/10.1016/j.oceaneng.2024.120046.
Tang, X., Huang, W., Li, X., Ma, G., 2025. Prediction of mooring tension of floating offshore wind turbines by CNN-LSTM-ATT and chebyshev polynomials. Ocean. Eng. 331, 121327. https://doi.org/10.1016/j.oceaneng.2025.121327.
Vaswani, A., Shazeer, N., Parmar, N., Uszkoreit, J., Jones, L., Gomez, A.N., Kaiser, Ł., Polosukhin, I., 2017. Attention is all you Need. 31st Conf. Neural Inf. Process. Syst., 2017. NIPS.
Wang, L., Robertson, A., Jonkman, J., Yu, Y.-H., 2022b. OC6 phase I: improvements to the OpenFAST predictions of nonlinear, low-frequency responses of a floating offshore wind turbine platform. Renew. Energy 187, 282–301. https://doi.org/10.1016/j.renene.2022.01.053.
Wang, Y., Chen, H., Koop, A., Vaz, G., 2022a. Hydrodynamic response of a FOWT semi-submersible under regular waves using CFD : verification and validation. Ocean. Eng. 258, 111742. https://doi.org/10.1016/j.oceaneng.2022.111742.
Wang, Y., Chen, H.-C., 2023. Verification and validation of computational fluid dynamic simulations of a FOWT semi-submersible under bichromatic and random waves. J. Offshore Mech. Arctic Eng. 145, 1–21. https://doi.org/10.1115/1.4056421.
Xie, Y., Tang, H., 2024. A deep learning approach based on domain generalization for mooring tension prediction in floating structures. Ocean. Eng. 306, 118128. https://doi.org/10.1016/j.oceaneng.2024.118128.
Xie, Y., Tang, H., Low, Y.M., 2023. Deep gated recurrent unit networks for time-domain long-term fatigue analysis of mooring lines considering wave directionality. Ocean. Eng. 284, 115244. https://doi.org/10.1016/j.oceaneng.2023.115244.
Xu, S., Xue, Y., Zhao, W., Wan, D., 2022. A review of high-fidelity computational fluid dynamics for floating offshore wind turbines. J. Mar. Sci. Eng. 10, 1357. https://doi.org/10.3390/jmse10101357.
Yan, J., Zhang, Y., Su, Q., Li, R., Li, H., Lu, Z., Lu, H., Lu, Q., 2023. Time series prediction based on LSTM neural network for top tension response of umbilical cables. Mar. Struct. 91, 103448. https://doi.org/10.1016/j.marstruc.2023.103448.
Yao, J., Wu, W., Li, S., 2022. Anomaly detection model of mooring system based on LSTM PCA method. Ocean. Eng. 254, 111350. https://doi.org/10.1016/j.oceaneng.2022.111350.
Ye, M., Cao, K., Wang, J., Wan, D., 2026. Mooring tension prediction of floating offshore wind turbines using end-to-end convolutional neural network models with attention mechanisms. Ocean. Eng. 346, 123939. https://doi.org/10.1016/j.oceaneng.2025.123939.
Ye, Y., Wang, L., Wang, Y., Qin, L., 2022. An EMD-LSTM-SVR model for the short-term roll and sway predictions of semi-submersible. Ocean. Eng. 256, 111460. https://doi.org/10.1016/j.oceaneng.2022.111460.
Yu, Y., Si, X., Hu, C., Zhang, J., 2019. A review of recurrent neural networks: LSTM cells and network architectures. Neural Comput. 31, 1235–1270. https://doi.org/10.1162/neco_a_01199.
Yuan, L., Chen, Y., Li, Z., 2024. Real-time prediction of mooring tension for semi-submersible platforms. Appl. Ocean Res. 146, 103967. https://doi.org/10.1016/j.apor.2024.103967.
Yuan, L., Chen, Y., Zan, Y., Zhong, S., Jiang, M., Sun, Y., 2023. A novel hybrid approach to mooring tension prediction for semi-submersible offshore platforms. Ocean. Eng. 287, 115776. https://doi.org/10.1016/j.oceaneng.2023.115776.
Zhang, M., Yuan, Z.-M., Dai, S.-S., Chen, M.-L., Incecik, A., 2024. LSTM RNN-based excitation force prediction for the real-time control of wave energy converters. Ocean. Eng. 306, 118023. https://doi.org/10.1016/j.oceaneng.2024.118023.
Zhao, L., Li, Z., Qu, L., Zhang, J., Teng, B., 2023. A hybrid VMD-LSTM/GRU model to predict non-stationary and irregular waves on the east coast of China. Ocean. Eng. 276, 114136. https://doi.org/10.1016/j.oceaneng.2023.114136.
Zhong, W., Zhao, W., Wan, D., Zhao, Y., 2024. Comparison study on mooring line models for hydrodynamic performances of floating offshore wind turbines. Ocean. Eng. 296, 117083. https://doi.org/10.1016/j.oceaneng.2024.117083.